Intranasal Delivery of Targeted Polyfunctional Gold-Iron Oxide Nanoparticles Loaded with Therapeutic microRNAs for Combined Theranostic Multimodality Imaging and Presensitization of Glioblastoma to Temozolomide

Uday K. Sukumar[1], **Rajendran J.C. Bose**[1], **Meenakshi Malhotra**[2], **Husam A. Babikir**[2], **Rayhaneh Afjei**[2], **Elise Robinson**[1], **Yitian Zeng**[4], **Edwin Chang**[3], **Frezghi Habte**[1], **Robert Sinclair**[4], **Sanjiv S. Gambhir**[3], **Tarik F. Massoud**[2,*], **Ramasamy Paulmurugan**[1,*]

[1]Cellular Pathway Imaging Laboratory (CPIL), Molecular Imaging Program at Stanford, Stanford University School of Medicine, 3155 Porter Drive, Palo Alto, CA 94305, USA;

[2]Laboratory of Experimental and Molecular Neuroimaging (LEMNI); Molecular Imaging Program at Stanford; Stanford University School of Medicine, 300 Pasteur Drive, Grant Bldg. S031, Stanford, CA 94305, USA;

[3]Multimodality Molecular Imaging Laboratory (MMIL), Molecular Imaging Program at Stanford; Stanford University School of Medicine, Clark Center, 318 Campus Drive, Stanford, CA 94305, USA.

[4]Department of Materials Science and Engineering, Stanford University, Stanford, California 94305-4034, United States

Abstract

The prognosis for glioblastoma (GBM) remains depressingly low. The biological barriers of the brain present a major challenge to achieving adequate drug concentrations for GBM therapy. To address this, we explore the potential of the nose-to-brain direct transport pathway to bypass the blood-brain barrier, and to enable targeted delivery of theranostic polyfunctional gold-iron oxide nanoparticles (polyGIONs) surface loaded with therapeutic miRNAs (miR-100 and antimiR-21) to GBMs in mice. These nanoformulations would thus allow presensitization of GBM cells to the systemically delivered chemotherapy drug temozolomide (TMZ), as well as *in vivo* multimodality molecular and anatomic imaging of nanoparticle delivery, trafficking, and treatment effects. First, we synthesized GIONs coated with β-cyclodextrin-chitosan (CD-CS) hybrid polymer, and co-loaded with miR-100 and antimiR-21. Then we decorated their surface with PEG-T7 peptide using CD-adamantane host-guest chemistry. The resultant polyGIONs showed efficient miRNA loading

with enhanced serum stability. We characterized them for particle size, PDI, polymer functionalization, charge and release using dynamic light scattering analysis, TEM and qRT-PCR. For *in vivo* intranasal delivery, we used U87-MG GBM cell-derived orthotopic xenograft models in mice. Intranasal delivery resulted in efficient accumulation of Cy5-miRNAs in mice treated with T7-targeted polyGIONs, as demonstrated by *in vivo* optical fluorescence and MR imaging. We measured the therapeutic response of these FLUC-EGFP labeled U87-MG GBMs using bioluminescence imaging. Overall, there was a significant increase in survival of mice co-treated with T7-polyGIONs loaded with miR-100/antimiR-21 plus systemic TMZ, compared to the untreated control group, or the animals receiving non-targeted polyGIONs-miR-100/antimiR-21, or TMZ alone. Once translated clinically, this novel theranostic nanoformulation and its associated intranasal delivery strategy will have a strong potential to potentiate the effects of TMZ treatment in GBM patients.

Keywords

Gold Iron Oxide Nanoparticles; miRNA therapeutics; cancer nanotheranostics; Glioblastoma; molecular imaging; luciferase; MR imaging

Introduction

Glioblastoma (GBM) is the most malignant primary brain tumor and the 12th leading cause of cancer-related deaths in the USA [1]. Despite conventional multimodal treatments that include surgery, radiation therapy, and chemotherapy (primarily temozolomide, TMZ), the median survival rate of patients remains at 14.6 months after diagnosis [2, 3]. As most chemotherapeutic drugs fail to cross the blood-brain barrier (BBB), the overall effectiveness of drug treatments remains poor [4]. In contrast to existing chemotherapeutic drugs that have limited success in targeting diverse GBM cell populations, a more specific and personalized treatment, such as silencing the expression of genes associated with the disease by using RNA interference therapy, may provide potentially useful and biologically meaningful avenues to treat GBM [5]. MicroRNAs (miRNAs or miRs) are small (18–22 nucleotides) non-coding RNAs that regulate gene expression by binding to partially or fully complementary recognition sequences of target messenger RNA (mRNA), resulting in mRNA degradation or translational suppression [6]. By negatively regulating their target mRNAs, miRNAs can act as either tumor suppressors or oncogenes (oncomiRs). Furthermore, unlike siRNAs where a single siRNA may be used to silence one target mRNA, a single miRNA can target a large number of genes involved in a specific regulatory pathway.

The tumor suppressor p53 plays a central role in preventing development and progression of GBM [7]. Numerous miRNAs that have an impact on the p53 network (e.g. miR-21) are dysregulated in GBM, leading to enhanced gliomagenesis, as well as chemo- and radiotherapy resistance. MiR-21 has been identified as a potent oncomiR overexpressed in the majority of GBMs and regulating important target genes involved in the apoptotic pathway [8–11]. In contrast, miR-100 is under-expressed in GBM cells and contributes to tumorigenesis [12, 13]. Overexpression of miR-100 suppresses cell proliferation and induces

apoptosis and cell cycle arrest in tumor cells by targeting multiple tumor-related genes that include polo like kinase 1 (PLK1), a pivotal regulator of mitosis and cytokinesis [14, 15]. PLK1 inhibition results in preferential cell death of p53 defective cells, which are found in 85–90% of glioma grade IV primary glioblastoma [16–18].

Thus, it would be advantageous to investigate the combined therapeutic effect of miR-100 and antimiR-21 in improving TMZ therapy, which is the present fist line standard clinical therapeutic drug for GBM patients, especially on p53 wildtype and mutant GBM cells.

Synthetic naked miRNAs rapidly degrade in plasma. To improve the delivery of synthetic miRNA mimics and antisense miRNAs in patients, and to reduce their degradation in the systemic circulation, various delivery systems have been proposed for clinical translation. Nanoparticles, with their unique size, shape and surface properties, are under intense scrutiny as potential drug and gene delivery platforms to the brain. The preferential accumulation of some nanoparticles in tumors and their ability to encapsulate and deliver therapeutic molecules in a 'Trojan horse' fashion by surface engineering with targeting peptides or antibodies makes them attractive candidates for miRNA delivery to GBMs. The translation of the concept of delivering small biomolecules (e.g. miRNAs or antisense miRNAs [antimiRs]) into the clinic is however limited by the barriers (BBB, and blood-tumor barrier) to delivery, which are unique and promising when targeting the brain [19]. The BBB is characterized by the presence of tight junctions between the cerebral vascular endothelial cells, guarding blood-borne compounds from selective diffusion and entering the brain [20]. Thus, current strategies include invasive techniques that mechanically breach the BBB to deliver drugs, such as intra-cerebro-ventricular delivery or convection-enhanced delivery [21]. In contrast to these complicated invasive approaches, the conceptually appealing approach of intranasal delivery of therapeutics to the brain is emerging as a non-invasive technique that bypasses the BBB.

The biggest advantage of the intranasal delivery route over the parenteral route is that it also avoids elimination by liver, gastrointestinal tract, serum degradation, and kidney filtration [22]. Upon intranasal administration the extensive mucosal epithelium provides the initial absorption site for subsequent passage of therapeutics across the nasal epithelium by two different pathways, either intracellular and/or extracellular. The extracellular transport includes passive transport across the nasal epithelium, which is comparatively the faster route and also serves as a primary mechanism for transport of therapeutics to the brain. The intracellular pathway includes endocytosis of the drug into olfactory and trigeminal nerve branches followed by axonal transport into brain. Olfactory nerves provide access to the cerebrospinal fluid (CSF) and the olfactory bulb in the fore region of the brain, whereas the trigeminal nerves provide access to the hind region of the brain in the brainstem.

The nanoparticles can travel along the trigeminal nerves in endocytic vesicles via the ophthalmic and maxillary divisions, to arrive into the brain. Thus, the intracellular pathway is apparently one route, but not the primary route. Conversely, the extracellular pathway (also called paracellular pathway) occurs along olfactory or trigeminal nerves by bulk flow processes in which the nanoparticles cross the epithelial layer, and upon reaching the lamina propria, the nanoparticles permeate through the tight junctions to reach the cleft between the

axons and the unsheathing layer. The high neuronal turnover within the olfactory epithelial layer renders the tight junctions permeable to nanoparticles to allow reaching the perineural channels surrounding the olfactory and trigeminal nerves [23, 24].

Here, we investigate intranasal delivery of molecularly-targeted theranostic nanoformulations against GBM. We thus develop and characterize a novel theranostic polyfunctional gold-iron oxide nanoparticle (polyGION) to deliver antimiR-21 and miR-100 that selectively target and counter GBM, and improve the therapeutic outcome of concomitant TMZ chemotherapy. PolyGIONs surface functionalized with chitosan-cyclodextrin (CD-CS) hybrid polymers provide an efficient platform for surface loading of negatively charged miRNAs through electrostatic interaction, while also effectively limiting the size of nanoparticles below 50 nm to fulfill the prerequisite size criterion for efficient intranasal delivery. Moreover, to be of value as therapeutic agents, the targeted delivery of polyGIONs, and visualization of their trafficking would be essential. Hence, we here develop and experimentally validate the intranasal delivery of GION core-shells (that enable MR imaging), coated with GBM cell-targeting T7 peptide, functionalized with conjugated CD-CS hybrid polymer, and pre-loaded with miRNAs (antimiR-21 and miR-100) as an effective theranostic system against GBM. The mucoadhesive chitosan facilitates adhesion to the nasal mucosa upon inhalation. We pre-clinically evaluate this nanoformulation after intranasal delivery in mice bearing orthotopically implanted GBMs, and find prominent suppression of GBM proliferation and concurrent improvement in animal survival rates. Furthermore, the presence of polyGIONs enables simultaneous multimodality imaging of intranasal delivery and trafficking to intracranial tumors. The non-invasive intranasal targeted delivery of therapeutic miRNAs using this polyGION nanoformulation offers a potentially exciting new avenue to improve treatment options for GBM (Scheme 1).

Results and Discussion

Design, Synthesis and Physicochemical Characterization of PolyGIONs: Synthesis of Cyclodextrin Conjugated Chitosan and T7-PEG-Adamantane Precursors.

We prepared cyclodextrin conjugated chitosan derivatives (C6 substituted) (CTS-en-CD) by nucleophilic substitution of CDen on 6-OTs-chitin, followed by the removal of acetyl groups on the chitin main chain (Figure 1A). The Fourier-transform infrared spectroscopy (FTIR) spectra of chitin, 6-OTs-chitin, chitin-en-CD, and CTS-en-CD are shown in Figure 1B. In the IR CD-OTs-6 presented a characteristic peak of benzene cycle backbone (Ts groups) vibration at 1594 cm^{-1} and the bending vibration at 812.5 cm^{-1}, which clearly indicated that β-CD had reacted with TsC1. Furthermore, in the subsequent steps, the benzene cycle backbone associated peaks (at 1594 cm^{-1} and 812.5 cm^{-1}) disappeared from the FTIR spectrum of CDen owing to Ts groups leaving the β-CD-OTs-6 when β-CD-OTs-6 reacted with chitin derivative (i.e. CTN-6-OTs). Comparing the FTIR spectra of chitin and 6-OTs-chitin shows that the 1602 cm^{-1} absorption peak resulted from stretching vibration of the benzene ring, while the C-H bending vibration of the benzene ring were assigned at 811 cm^{-1} and 677 cm^{-1}. The asymmetrical stretching vibration for the S=O bond of the tosyl group appeared at 1347 cm^{-1} and the corresponding symmetrical stretching vibration peak

appeared at 1175 cm^{-1}, indicating that the tosyl groups were immobilized on the C6 position of the pyranose ring.

After nucleophilic substitution with CDen, the absorption peaks at 1347 cm^{-1} and 1175 cm^{-1} from the tosyl group disappeared. Furthermore, the absorption peak at 1602 cm^{-1} resulting from the stretching vibration of the benzene ring disappeared and was accompanied by significant decline in absorption peak, corresponding to bending vibration of the benzene ring at 811 cm^{-1} and 677 cm^{-1}. The stretching vibration at 3420 cm^{-1} assigned to -OH appeared enhanced and broadened. The peak at 1640 cm^{-1} also became broader owing to the bending vibration of water absorbed by cyclodextrin. The peak at 1430 cm^{-1} assigned to the bending vibration of O-H and the peak at 1156 cm^{-1} from the stretching vibration of C-O-C were both increased. All of these observations indicated that p-toluene sulfonyl ester on the C6 position of chitin was displaced by nucleophilic substitution with CDen. The subsequent step of acetyl group removal from chitin-en-CD led to appearance of the absorption peak at 1596 cm^{-1}, corresponding to the bending vibration of the amide bond. This was also accompanied by a marginal decrease shift in C=O peak at 1664 cm^{-1}. The major absorption peaks characteristic of cyclodextrin remained unchanged. Therefore, the FTIR results clearly showed that we obtained the desired product (CTS-en-CD) after deacetylation of chitin-en-CD.

The T7 heptapeptides conjugation with MAL-PEG-NHS (activated N hydroxysulfosuccinimide ester of PEG) was achieved by successful completion of the reaction between the terminal thiol group of cystine in T7 peptide (Ac-Cys-His-Ala-Ile-Tyr-Pro-Arg-CONH$_2$) and the MAL group of MAL-PEG-NHS (Figure 1C). The consecutive peaks separated by 44 amu corresponded to the [-CH$_2$ -CH$_2$ -O]$_n$- repetitive unit of PEG. Upon conjugation of T7 and adamantane to its terminal groups, the peaks shifted to the right by ~1054 amu, of which 997 amu was contributed by the peptide. The remaining 57 amu depicted the presence of adamantane, which validates the successful synthesis of T7-PEG-adamantane conjugate (Figure 1D).

Synthesis and Characterization of MiRNA-Loaded Cyclodextrin-Chitosan-PolyGIONs.

We prepared T7 functionalized cyclodextrin-chitosan (CD-CS)-polyGIONs loaded with antimiR-21 and miR-100 through a sequence of steps shown schematically in Figure 2A–B. The negatively charged GION nanostars were prepared by consecutive seed and growth steps which led to uniform sized particles of 31.3 ± 20 nm and −15 mV surface potential (Figure 2C). The TEM images of the prepared gold-iron oxide nanostars confirmed the presence of GIONs of uniform size distribution of 34 ± 15 nm, and demonstrated the regular spiked surface morphology of the nanostars. Furthermore, EDX analysis of the GION nanostars confirmed the presence of iron in the core and gold spikes on its surface (Figure 2D, E). The uniform sized iron oxide nanoparticles (15 ± 5 nm) synthesized by a microwave-assisted precipitation method served as seeds for GION nanostars synthesis. These underwent morphological changes with subsequent growth of the gold phase on their surface, as a result of which we observed a broad plasmon absorption band in the NIR region (with an absorption maximum at 825 nm) for GION nanostars. This absorption band was absent in the pristine iron oxide nanoparticles UV-Vis spectra (Figure 2F). The localized

electromagnetic field enhancement in the branched gold tips led to the observed broad absorption band that was otherwise absent in spherical gold nanoparticles.

The partial negative surface potential of GION nanostars facilitated electrostatic deposition of positively charged CD-CS polymer phase on their surface, which we inferred from DLS measurements showing shift in size of the particles from 31.3 nm to 42.6 nm. Apart from an increase in size of the particles, upon inclusion of CD-CS coating on GION nanostars, the surface potential of these particles also shifted from –15 mV to 39 mV owing to excess of positively charged free amine groups of chitosan on the surface of GION nanostars. Inclusion of the CD-CS polymer phase precomplexed with miRNA on the surface of GION nanostars resulted in particles of similar size, i.e. 44.5 nm. However, they possessed a lower surface potential of 16 mV as compared to CD-CS coated GION nanostars (39 mV), indicating that the presence of miRNAs loaded in the polymer phase led to partial neutralization of the positive charges on the surface of the nanoparticles. Subsequent inclusion of T7 peptide on the surface of miRNA-loaded CD-CS phase using CD-adamantane host-guest chemistry led to an increase in particle size from 44.5 nm to 53.2 nm, and masked the surface potential to result in a decline to 3.8 mV. The supramolecular interaction between CD and adamantane-T7 peptide drove the surface functionalization step. This also provided a versatile means of controlling the targeting peptide on the surface of the nanoparticles by just varying the proportion of host and guest.

To assess the stability of nanoparticles over the course of storage at 4 °C, we performed DLS estimation of T7-CD-CS-polyGION nanoparticles 4 weeks after initial synthesis and evaluated its size distribution and polydispersity index (Figure S2 **&** Table S1). We observed that the size and polydispersity index of nanoparticles changed very little upon storage at 4 °C, indicating that no significant instance of aggregation occurred after capping of NPs with CD-CS polymer phase. The TEM images of GION nanostars showed a stable and uniform polymer phase coated on their surface.

In the cell culture studies described below, we adapted this ratiometric combination method to identify the optimal levels of T7 functionalization for efficient cellular uptake. The gel retardation assay for polyGION miRNA encapsulation efficiency revealed that with increasing concentrations of CD-CS, the miRNA electrophoretic migration was retarded successively, clearly indicating the significance of electrostatic interaction in miRNA encapsulation (Figure 2G). The optimal ratio of 4 μg CD-CS complexed with 2 pmol miRNA was adopted for further *in vitro* and *in vivo* studies. We further extrapolated this observation in terms of quantitative electrophoretic mobility assessment of complexes made from different ratios of CD-CS to miRNA loaded in each lane (Figure 2G **and** Figure S3). With increase in CD-CS content, the electrophoretic mobility of bare miRNA declined from −5.406 μmcm/V (lane 1) to −0.543 μmcm/V when complexed with 7 μg CD-CS (Figure 2G **lane 8**). Although miRNAs are efficiently encapsulated in the CD-CS polymer phase, the susceptibility of loaded miRNA to RNase enzymes becomes a crucial factor governing its therapeutic effects. The RNase protection assay of CD-CS encapsulated miRNA indicated that CD-CS not only efficiently encapsulated the miRNA but also restricted RNase accessibility to loaded miRNAs, and thereby preserved the functional attributes of antimiR-21 and miR-100 to achieve their therapeutic effects. CD-CS loaded miRNA

quantification after preincubation with RNAase enzyme revealed that 87.4% of the loaded RNA remained intact, whereas bare miRNA subjected to RNase treatment for equivalent amount of times degraded >80% of miRNA (Figure 2G).

Estimation of microRNA loading and release form CD-CS-polyGION nanoparticles.

The therapeutic effects of miRNA delivery by CD-CS polyGIONs relies on the miRNA loading efficiency and stability during the synthesis procedure. We therefore assessed the efficiency of miRNA payload incorporation into the CD-CS hybrid polymer at each phase of the synthesis procedure, which includes initial encapsulation in CD-CS polymer phase and subsequent steps of GION surface capping, and during T7 surface functionalization (Table 1). We determined by precise quantitative RT-PCR analysis of miRNA-loaded CD-CS that $78.0 \pm 5.6\%$ of 1 nmol miRNA was complexed effectively by 2 mg of CD-CS hybrid polymer. The strong encapsulation efficiency arose from the cationic nature of chitosan, which enabled easy and fast complex formation with negatively charged miRNA. In the subsequent step, the miRNA-loaded CD-CS complexes having partial net positive charge were interlaced onto the surface of GION nanostars by electrostatic interaction. The quantitative estimation of magnetically separated GIONs capped with miRNA-loaded CD-CS revealed successful loading of $82.89 \pm 8.14\%$ miRNA. Correlation of obtained Ct values to the standard plot for antimiR-21 indicated 3.89×10^{14} copies of miRNA in the loaded 2 mg of CD-CS-polyGION-miRNA complex. Simultaneous estimation of GIONs concentration by NTA at this stage led to a value of 2.0×10^9 nanoparticles in each 20 μL (Figure S1, Video S1, S2 **&** S3). Correlation of miRNA copy number with GION concentration furthered enabled us to deduce that 6424 ± 83 copies of miRNAs were loaded on each CD-CS polyGIONs. Incorporation of T7 tagged PEG-adamantane conjugate moieties on the surface of nanoparticles did not hamper the nanoparticle recovery or miRNA loading efficiency in CD-CS capped GIONs, which was determined to be 6746 ± 134 copies of miRNA on each GION. Thus, 20 μL of this nanoformulation administered to the animal at each time point of our *in vivo* study comprised 2.006×10^9 CD-CS-polyGIONs (58.9 μg of CD-CS and 19.6 μg of T7-adamantane-PEG) loaded with 1.35×10^{13} copies of miRNA, i.e. 22.18 pmol miRNA.

We evaluated the time dependent miRNA release from CD-CS-polyGIONs at different pH values (i.e. pH = 5.5, 6.5 and 7.5) at 37 °C in a rotary shaker for 72 h. Overall, the miRNA release profile followed a generalized trend that included an initial increase in miRNA release until 12 h, ultimately receding gradually until 72 h. The initial phase of miRNA release from the CD-CS nanoparticles was predominantly driven by swelling of the polymer, and diffusion of loosely bound miRNA from the polymer phase, whereas the later release phase with slow and constant release profile was plausibly driven by dissociation of miRNA-loaded CD-CS from the GION surface. The improved solubility of chitosan at pH 5.5, accompanied by higher swelling and dissolution, led to marked increase in miRNA release when compared to that at pH 6.5 and pH 7.5 at any given time point. The pH dependent variation in release profile was much more prevalent in the initial phase until 24 h (i.e. 2.56-fold, 2.44-fold, and 2.38-fold higher micro release at pH 5.5, as compared to that at pH 7.5; at 8 h, 12 h, and 24 h, respectively), whereas the difference gradually narrowed down to 7.3% between pH 5.5 and 7.5 at 72 h. This observation further confirmed the role of pH-

dependent solubility and swelling of chitosan, which instigates miRNA release and dissolution from the CD-CS polyGIONs. Consequently, the CD-CS polyGIONs trigger higher miRNA release within the relatively acidic milieu of cancer cells. Aside from elucidating the release profile, our study also established the stability of the miRNA payload on the nanoparticles (Figure S4).

T7-Functionalized CD-CS-PolyGIONs Improved Cellular Uptake of miR-100 and AntimiR-21 in GBM Cells.

We evaluated the uptake of miRNA-loaded CD-CS-polyGIONs in human GBM cells (U87-MG) qualitatively using fluorescent microscopy, and quantitatively using flow cytometry and qRT-PCR assay. We assessed nanoparticle delivery using Cy5-antimiR-21 and miR-100 loaded in the CD-CS layer of polyGIONs; the presence of fluorescent tag Cy5 enabled us to effectively track and quantify the extent of nanoparticle internalization in cells in a time-dependent manner. The exogenous non-targeted nanoparticles were internalized by non-specific passive transport across the cell membrane. Inclusion of targeting peptide T7 on the surface of these nanoparticles further augmented cellular internalization by receptor mediated endocytosis of targeted nanoparticles (Figure 3). The uptake level of T7-targeted and non-targeted polyGION nanoparticles was assessed in U87-MG cells at 4, 8, 12 and 24 h post incubation both with and without preincubation with T7 peptide (as a means of blocking T7 mediated uptake of nanoparticles) (Figure S5). At every time point of analysis, the cellular uptake level of Cy5-miRNAs was higher in the case of T7 functionalized nanoparticles. For instance, at 4 h, mean Cy5 fluorescence of internalized miRNA was 1120 au in case of non-targeted nanoparticles, whereas in the case of T7 targeted nanoparticles, mean Cy5 fluorescence intensity of cells was 2045 au. Thus, with significance of $p<0.0001$ T7-mediated targeting increased cellular uptake in U87-MG cells by 1.82 fold higher at 4 h of incubation. Furthermore, in order to validate that the observed difference was an outcome of T7-mediated uptake, we preincubated the U87-MG cells with T7 peptide to block the receptors and then incubated with T7 targeted nanoparticles. As a consequence, we observed that the difference was reversed, and the cellular uptake levels were similar to those of non-targeted polyGION. This observation clearly strengthens the claim that T7 plays a major role in uptake of T7-polyGION nanoparticles.

The miRNA-loaded CD-CS-polyGIONs that we used had a net positive charge. This facilitated passive diffusion across the membrane when these nanoparticles were adsorbed on the cell membrane owing to the latter's inherent negative membrane potential. Consequent to such non-specific adsorption, plus the electrostatic interaction driven transport, there were significantly higher levels of miRNA internalization when loaded on CD-CS-polyGIONs as compared to bare miRNAs. The surface modification of these nanoparticles with T7 peptide further improved the nanoparticle internalization by targeting the transferrin receptor-mediated endocytosis in cancer cells. The transferrin receptor is overexpressed in GBM cells [25]. We observed higher levels of intracellular miRNA delivery when U87-MG cells were treated with T7-targeted CD-CS-polyGIONs loaded miRNAs as compared to their non-functionalized counterparts at every time point during our observations (Figure 3A–C **and** Figure S5). Flow cytometry analysis of the treated cells at the end of 48 h further revealed the quantitative differences in miRNA uptake levels upon

encapsulation in CD-CS-polyGIONs, and its further improvement by using T7 functionalization (Figure 3C). We observed in cell populations treated with T7 peptide functionalized polyGIONs that there were significantly ($P < 0.05$) higher levels of fluorescence signal compared to cells treated with non-targeted CD-CS-polyGIONs. Our results further corroborate that T7 targeting improved miRNA delivery in U87-MG cells. The cells treated with non-targeted polyGIONs showed a clear increase in miRNA levels compared to bare miRNA treated cells, but much lower than with use of targeted nanoparticles. Thus, our findings confirmed efficient loading of miRNAs in CD-CS-polyGIONs and their delivery to GBM cells.

We also investigated three different variants of targeted CD-CS-polyGIONs with different extents of T7 functionalization on their surface to identify the optimal level of T7 functionalization required for efficient delivery. As illustrated in the nanoparticle synthesis scheme (Figure 2A), the high affinity supramolecular interaction between cyclodextrin and adamantane moieties drives the T7 functionalization on the surface of CD-CS-polyGIONs. The ease and specificity of this functionalization step offers a feasible means of tuning the extent of T7 functionalization on the surface of CD-CS-polyGIONs for effective receptor mediated endocytosis by U87-MG cells. Thus, we investigated cellular uptake levels of CD-CS-polyGIONs functionalized with three different ratios of CD-CS with respect to T7-adamantane, i.e. 1:1, 1:2 and 1:3 ratios (Figure 3C). We found that although cellular uptake did rise with an increase in T7 surface functionalization, i.e. from 1:1 to 1:2, at a ratio of 1:3 the nanoparticle uptake was significantly diminished ($P < 0.05$). Further analysis of size and charge of these nanoparticles revealed that the higher extent of T7 functionalization led to an increase in size of the nanoparticles from 53 nm to 65 nm owing to higher instance of CD-adamantine interaction. Aside from changes in nanoparticle size and surface potential, the observed differences in cellular uptake may possibly arise from the effect of T7 peptide-receptor recognition. Indeed, the presence of excess T7-peptide could lead to steric hindrance in receptor recognition, which could destabilize the binding affinity of ligand with the receptor.

CD-CS-polyGIONs co-loaded with GION nanostars also facilitated simultaneous uptake of GIONs, as assessed by Prussian Blue staining (Figure 3B). We showed in the miRNA uptake results that we achieved the highest labeling in cells treated with T7 functionalized CD-CS-polyGIONs, followed by marginally lower levels in non-targeted polyGIONs. Moreover, when using CD-CS-polyGIONs, a significant fraction of nanoparticles was still present in the extracellular space, and even those internalized by the cells were dispersed in the cytoplasm. However, when using T7 functionalized CD-CS-polyGIONs, large clusters of nanoparticles were concentrated in specific cell organelles. We subsequently used the optimized formulation of T7 functionalized CD-CS-polyGIONs for co-delivery of antimiR-21 and miR-100 in U87-MG cells. We quantified the extent of miRNA delivery using TaqMan qRT-PCR analysis of treated cells at the end of 48 h (Figure 3D). Since antimiR-21 is absent in the endogenous miRNA expression profile of U87-MG cells, this enabled absolute quantification of the delivered levels of antimiR-21, in contrast to miR-100 where the endogenously expressed basal levels of miR-100 were quantified along with the delivered synthetic miR-100.

This miRNA quantitation revealed a nearly 8×10^5-fold increase in intracellular levels of antimiR-21 as compared to control cells; whereas for miR-100, the endogenous expression level increased to nearly 3-fold compared to control cells. We also validated the role of the targeting moiety T7 in cellular uptake of nanoparticles in terms of delivered miRNA levels. The T7 peptide functionalization could achieve approximately $8.8 \times 10^5 \pm 2.4 \times 10^3$-fold increase in antimiR-21, compared to approximately $4.7 \times 10^5 \pm 7.6 \times 10^3$-fold increase in the case of non-targeted CD-CS-polyGIONs. We observed similar extents of differences in the case of miR-100 expression levels, which increased from 1.4-fold to 2.8-fold upon inclusion of T7 peptide on CD-CS-polyGIONs. We also established that the levels of endogenous miR-21 (a direct target of antimiR-21) fell to nearly 15–20% of the endogenous levels in untreated control cells, thus fulfilling the therapeutic goal of delivering this miRNA. AntimiR-21 and miR-100 are vital regulators of apoptosis, proliferation, migration and drug sensitivity. In this study we further analyzed the role of these miRNAs in presensitizing GBM cells to augment the effects of the standard anti-GBM chemotherapy drug, TMZ.

AntimiR-21 and MiR-100 Presensitized GBM Cells to TMZ Chemotherapy *In Vitro*.

We tested the functional effects of antimiR-21 and miR-100 combinations (delivered using CD-CS-polyGIONs) in improving sensitivity of GBM cells to TMZ chemotherapy. We investigated in U87-MG cells the antiproliferative and cytotoxic effects of T7-targeted and non-targeted CD-CS-polyGIONs co-delivering antimiR-21 (50 pmol) and miR-100 (50 pmol), with or without TMZ (100 μM or 250 μM) treatment (Figure 3E). We pre-treated the cells with antimiR-21 or miR-100 loaded CD-CS-polyGIONs 24 h prior to TMZ treatment. We then tested cell viability after 48 h of TMZ treatment. At the end of 48 h, CD-CS-polyGIONs loaded with antimiR-21 or miR-100 alone reduced the cell viability to 27.9% and 29.9%, respectively, whereas the co-delivery of the antimiR-21 and miR-100 combination led to further decline in cell viability to 49.3%, indicating the concerted antiproliferative effects of both miRNAs against U87-MG cells. To assess the relative contributions of antimiR-21 and miR-100 mediated pre-sensitization of U87-MG cells to TMZ chemotherapy, we studied two different concentrations of TMZ, 100 μM and 250 μM, in combination with different CD-CS-polyGIONs loaded with antimiR-21 and/or miR-100. Co-treatment with 100 μM TMZ in combination with antimiR-21 or miR-100 independently resulted in 43.8% and 54.7% decline in cell viability compared to 31.2% by TMZ alone, which clearly indicated that both antimiR-21 and miR-100 independently augment the anticancer potential of TMZ against U87-MG cells. Additionally, co-supplementation of both miRNAs in combination with 100 μM TMZ led to further decline in cell viability to 39.2%, which clearly indicated that concomitant delivery of both miRNAs potentiates the TMZ anticancer efficacy more than the miRNAs individually. Of note, at the higher concentrations of TMZ (250 μM), we found that co-treatment with antimiR-21 and miR-100 brought about a decline in cell viability from 30.2% to 15.2%. However, when using 100 μM TMZ with the equivalent co-treatment using antimiR-21 and miR-100, the decline in cell viability was predominantly owing to the increase in TMZ dose alone, pointing to the fact that miRNA supplementation potentiates TMZ therapy much better at the lower concentrations (i.e. 100 μM) than at the higher concentrations (i.e. 250 μM). At these high concentrations, the antiproliferative effect is predominantly owing to the TMZ alone.

Although an increase in TMZ dosage alone from 100 μM to 250 μM brought about a decline in cell viability from 69.8% to 59%, co-treatment using antimiR-21 and miR-100 plus 100 μM TMZ reduced the cell viability to 39.2%. Thus, the effective therapeutic dosage of TMZ for GBM could be drastically reduced by supplementation with therapeutic miRNAs. In theory, this could constitute an important advantage, considering that systemic TMZ delivery to the brain is severely limited by the BBB during conventional GBM therapy [26]. Of note, in live/dead analysis of cells treated with combinations of TMZ plus antimiR-21 and/or miR-100, we found two distinct cell population subsets clearly distinguished by their nuclear content in the apoptotic region, pointing to the fact that miRNA pre-sensitization occurred by sequential induction of cell death through early and late apoptotic processes (Figure 3E).

AntimiR-21 and MiR-100 Co-Treatment Enhanced TMZ Therapy by Activating the Apoptotic Signaling Pathway in GBM Cells.

Next, we sought to elucidate the cellular signaling cascade involved in miRNA-mediated GBM pre-sensitization of TMZ therapy by assessing the expression levels of target proteins of antimiR-21 and miR-100 in the presence and/or absence of TMZ, and the consequent effects on apoptosis regulator proteins during such therapeutic enhancement (Figure 4A–H). MiR-21 overexpression in cancer is associated with drug resistance and poor response to chemotherapy from a compromised apoptotic mechanism in cancer cells. PTEN is a direct target of miR-21, and loss of PTEN by mutation, methylation, or deletion leads to decreased apoptosis [27]. Hence, using therapeutic antimiR-21, we aimed to upregulate PTEN levels by nullifying the function of endogenous miR-21 in GBM.

The endogenous overexpression of miR-21 is also a negative regulator of 'programmed cell death protein 4' (PDCD4), which is a well-established modulator of apoptosis and drug sensitivity. As shown earlier, CD-CS-polyGIONs efficiently delivered antimiR-21 to U87-MG cells, leading subsequently to suppression of endogenous miR-21 function. As a result, prominent upregulation of its direct target proteins occurred; PTEN and PDCD4 expression increased by 2.2-fold and 2.7-fold, respectively [28]. Alongside upregulation of direct targets of antimiR-21, pro-apoptotic protein Bax expression was also prominently upregulated by 2.8-fold, accompanied by marginal increase in the levels of caspase-3, indicating significant enhancement of the apoptotic pathway, and accounting for 29.9% decline in cell viability (p<0.001) (Figure 3E).

There is strong evidence that upregulation of PTEN and PDCD4 improves therapeutic response of cancer cells to diverse combinations of therapies [29, 30]. That prompted us to investigate any potential value with regard to anti-GBM TMZ therapy. We found that co-treatment of antimiR-21 plus TMZ brought about higher expression levels of PTEN and PDCD4, as compared to controls. This combination also increased the caspase-3 expression more than antimiR-21 or TMZ alone. There was therefore a prominent increase in apoptosis, accounting for the 54.7% cell death rate described earlier.

TMZ alone mediates cytotoxicity by introducing *a methyl group to the O-6 position of guanine (G) in genomic DNA, and subsequent futile cycles of DNA mismatch repair (MMR) system in removing GT mismatches leads to G2/M cell cycle arrest, cellular senescence and apoptosis; this is always preceded by accumulation of p53 and p21 proteins* [31, 32]. *We*

observed that the levels of p53 and p21 had increased approximately 2.2-fold and 1.8-fold, respectively, in U87-MG cells after 72 h exposure to a level of TMZ (i.e. 100 μM) that is well below its IC50 (IC50 of TMZ: 950 μM) (Figure 4C).

The crucial role of p53 in driving the TMZ therapeutic response converges with miR-100 mediated upregulation of p53 and caspase-3 through the mTOR pathway (miR-100 directly targets 3′UTR of mTOR in a post-transcriptional manner). As a direct manifestation of this convergence in signalling pathways, miR-100 improves the TMZ cytotoxicity by harnessing the combined outcome of caspase-3 and p53 mediated apoptotic signaling. Furthermore, miR-100 was identified previously as being significantly upregulated in radiosensitive GBM cells, and lately there is growing evidence that it plays a similar role in presensitization of GBM to chemotherapy. Our observed upregulation of p53 (~2-fold) upon presensitization of GBM using miR-100 prior to TMZ therapy is also a plausible outcome of the cumulative response of miR-100 mediated ATM regulation. The latter is also upregulated at low concentrations of TMZ, and drives the growth inhibition and apoptosis accompanied by activation of ATM and ATR kinase and phosphorylation of p53 [33]. *Our findings demonstrate a clear correlation between antimiR-21 and miR-100 mediated augmentation of TMZ therapy after co-delivery of both miRNAs (miR-100 and antimiR-21). This led to further improvement in therapeutic response as evidenced by the concomitant upregulation of p53 (3.2-fold), PTEN (1.3-fold), PDCD4 (1.8-fold) and caspase-3 (2.2-fold), which also correlated well with our observed trends in cell viability.*

Intranasal Delivery and Therapeutic Implication of MiRNA Loaded CD-CS-polyGIONs in TMZ Therapy of GBM.

We evaluated the delivery and therapeutic efficacy of miR-100 and anitmiR-21 loaded CD-CS-polyGIONs *in vivo*, in the presence and absence of TMZ (Figure 5A). For our study, we adopted a novel strategy of intranasal delivery of this nanoformulation along with an orthotopic GBM xenograft model of U87-MG cells. For tumor implantation, we used stable GBM cells constitutively expressing FLUC-EGFP in order to facilitate *in vivo* bioluminescence imaging as a cell or tumor viability marker. While the bioluminescence imaging enabled us to track GBM growth in response to treatment, the fluorescence of Cy5 dye tagged to the encapsulated miRNAs in the CD-CS-polyGIONs enabled real-time imaging of therapeutic nanodelivery throughout the study (Figure 5B).

We evaluated four treatment groups: the untreated control group, T7-CD-CS-polyGIONs-miRNA treated group, TMZ plus T7-CD-CS-polyGIONs treated group, and TMZ plus T7-polyGION-CD-CS-miRNA treated group. All mice, including the control group, received a fixed dose of TMZ (25 mg/kg) periodically. Acquisition of mouse fluorescence images under a Cy5 filter after every cycle of intranasal administration of the nanoformulation (CD-CS-polyGIONs-miRNA) showed consistent patterns in its *in vivo* trafficking. This started with initial accumulation in the nasal cavity as an outcome of the muco-adhesive nature of chitosan in CD-CS-polyGIONs, followed by gradual absorption through the nasal mucosa to enter perivascular spaces via branches of the olfactory and trigeminal nerves, to reaching the intracranial cavity in the following 24–48 h. As evident in all miRNA loaded CD-CS-polyGIONs treated cohorts, the tumor associated bioluminescence signal continued to

increase at a rate similar to control mice until the second dose of CD-CS-polyGIONs loaded with miRNAs reached the brain. We treated the control mice with equivalent amounts of bare Cy5 tagged miRNAs and TMZ, which began to decline over a treatment duration, but did so significantly to a lesser extent compared to CD-CS-polyGIONs-miRNA plus TMZ. After 24 h of administering the first dose of CD-CS-polyGIONs, fluorescence imaging clearly indicated progressive accumulation of nanoparticles in the prefrontal cortex of each mouse, and this continued over the subsequent 6–8 days. Although the first dose of CD-CS-polyGIONs-miRNA ultimately localized in the brain, they did not manifest any significant difference in tumor optical bioluminescence when compared to TMZ alone treated mice. However, upon administering the second intranasal dose of CD-CS-polyGIONs-miRNA, the tumor bioluminescence began to decline, especially seen with the greater reduction in the case of T7-targeted CD-CS-polyGIONs-miRNA group when compared to TMZ alone treated mice. This was evidence of a successful therapeutic outcome of miRNA augmented anti-cancer TMZ therapy against GBM when using our approach (Figure 5A–E). In contrast to these two cohorts, in bare miRNA treated mice, the Cy5 fluorescence remained localized in the nasal cavity for a short duration and then declined. These mice ultimately did not survive beyond 33 days of treatment. In sharp contrast, the mice treated with T7 targeted polyGIONs not only showed inhibition of tumor growth but also survived beyond 44 days; we subsequently euthanized these mice upon completion of the study (Figure 5C). Progression in tumor growth led to weight loss prior to mouse mortality. The weight loss was significantly delayed in the case of CD-CS-polyGIONs-miRNA and T7 targeted CD-CS-polyGIONs-miRNA treated mice, which also correlated well with the health status of these mice indicating tumor growth suppression (Figure 5D).

With the promising therapeutic outcome in the T7-targeted CD-CS polyGION treatment group, we conducted a separate study to assess the implication of T7-mediated targeting in improving the delivery and therapy of polyGIONs *in vivo* (Figure S5). The study involved mice grouped into three treatment regimes: untreated controls, non-targeted polyGIONs treated, and a T7-functionalized polyGIONs administered group. Both the polyGION treatment groups received 25mg/kg TMZ periodically. As an interesting outcome of this study we observed that the T7-targeted polyGIONs were retained over a prolonged period in the brain in comparison to when non-targeted polyGIONs were used. At the early stage of intranasal administration of nanoparticles, both targeted and non-targeted nanoparticles home into the brain but over the course of time only T7-functionalized nanoparticles were predominantly retained in the brain in comparison to non-targeted nanoparticles, which also show progressive accumulation in the lungs and kidney. As an outcome of this improved T7-mediated delivery, we also observed appropriate tumor response to the therapeutic miRNAs. As in the case of our earlier study (Figure 5B), the control mice could not survive beyond 16 days, whereas use of the T7-targeted polyGIONs showed good tumor suppression and improved survival. The T7-targeted polyGIONs were able to achieve ~42% reduction in tumor volume when compared to use of the non-targeted counterpart showing only a ~7.8% reduction in tumor volume over the course of 24 days' treatment. The results well substantiate the observations made in the *in vivo* study delineating the role of T7 in enhancing cellular uptake levels of U87-MG cells.

In vivo MRI, microCT and *Ex Vivo* Tissue Characterization Further Support the Delivery and Therapeutic Outcome of Intranasally Delivered MicroRNA (AntimiR-21 and MiR-100) Loaded CD-CS-polyGIONs in Improving TMZ Chemotherapy in GBM.

In addition to *in vivo* bioluminescence and fluorescence imaging we also used the MR signal property of gold- iron oxide nanostars for tracking the delivery of CD-CS-polyGIONs using MR imaging. We monitored the diagnostic component, i.e. GION nanostars at the core of polyGIONs, with 3T MRI head scans of treated mouse cohorts, using axial and coronal spin-echo T1-weighted sequences (Figure 6A). Prominent T1-shortening indicating nanoparticle-induced contrast enhancement in the right cerebral hemispheres coincided with the regions of intracranial tumor implantation and miRNA fluorescence showing accumulation of GION nanoparticles in GBMs. This accumulation was much more pronounced for T7-targeted CD-CS-polyGIONs as compared to the non-targeted nanoparticles. Sequential sections of coronal and axial images illustrated a specific pattern in the migration of GION nanostars, which delineated the nose-to-brain pathway taken by polyGIONs. Intranasally administered material first accumulates in nasal sensory neurons, Grueneberg ganglia, septal organs, olfactory epithelium, and ventro-nasal organs. These eventually propel this material into the rostral migratory stream (RMS) and olfactory tract at the base of the brain. The polyGIONs trafficking along the RMS reach the lateral and third ventricles in close proximity to the hippocampus, whereas those trafficking along the trigeminal nerves also reach the hindbrain near the fourth ventricle [34–36].

Furthermore, head microCT scans of mice enabled us to precisely track the course of polyGION migration into the brain upon intranasal administration (Figure S7). The intranasally administered polyGIONs generated bright hyperdense punctate foci in high resolution head scans, which enabled us to track the course of nanoparticles from the nose to brain. Figure S7(A&B) shows the accumulation of polyGIONs throughout the margins of olfactory epithelium indicating the retention of polyGIONs in the nasal mucosa. We also confirmed the same finding using Prussian Blue staining of nasal mucosa (Figure S7 E). Further, Figure S7(C) provides a possible evidence of passive transport of polyGIONs by olfactory nerves (axonal transport) into the olfactory bulb in the forebrain region. The *ex vivo* fluorescence imaging of miRNAs in the brains of treated mice presented in Figure 6B also indicated the accumulation of miRNA in the olfactory bulbs. Figure S7(D) delineates the adhesion of polyGIONs in the respiratory epithelium and the trigeminal nerves which lends access to the pons and medulla in the hindbrain. As evidence of this transport phenomenon, *ex vivo* fluorescence imaging in Figure 6(D) also indicated higher accumulation in the hindbrain. The trigeminal (V) nerve is the largest cranial nerve, branching into ophthalmic, maxillary and mandibular divisions. The ganglionic branches of the maxillary nerve include sensory fibers from the mucous membranes of the nose that are also reported to be involved in the delivery of therapeutics from the nasal cavity to the hindbrain. Although in the past different groups have reported delivery of metallic or polymeric nanoparticles to the brain by intranasal administration, a clear elucidation of the intranasal pathway using an imaging technique had not been established to date [37–39]. In the present work, using microCT we were able to successfully illustrate major transport pathways, that is, axonal transport via the olfactory and trigeminal nerves, as well as paracellular transport across the nasal epithelium.

Tumor bioluminescence images of mice brains and fluorescence images of all major organs harvested from mice in each treatment cohort upon completion of the treatment protocol are summarized in Figure 5A. The Cy5 fluorescence signal depicted predominant accumulation of CD-CS-polyGIONs in the brains of mice, apart from significant fractions distributed into the major organs including lungs, liver, spleen and kidney Figure 6B. Among these major organs, lungs showed strong presence of miRNAs, which is likely because intranasal delivery also allowed the nanoparticles to reach the lungs. Indeed, we found that an important factor in restricting intranasal nanoparticle migration into the respiratory tract was the rate of breathing during the intranasal administration in mice. We observed that under deep anesthesia, the slow breathing rate improves nanoparticle residence time in the nasal mucosa (the Cy5 fluorescence) which subsequently led to better absorption through the nasal mucosal and transition into the nose-to-brain pathway. By contrast, under light anesthesia, accompanied by relatively fast breathing rates and short intranasal residence time, the nanoparticles were not effectively absorbed in the nasal cavity. Aside from this, a consistent pattern in miRNA distribution was observed in the brains of mice. The delivered miRNAs were significantly concentrated in the rostral and caudal regions of the brain, clearly indicating that the nanoparticles administered intranasally had successfully trafficked along the pathways described above. Although, Cy-5 fluorescence signal was prevalent in the brain of non-targeted CD-CS-polyGIONs as well as targeted CD-CS-polyGIONs treated mice, the T7 targeted CD-CS-polyGIONs showed relatively better co-localization to tumors.

We also evaluated the quantitative changes in levels of miRNAs delivered to the mice brains and other organs using RT-PCR analysis for both antimiR-21 and miR-100 (Figure 6C, D). Validating our fluorescence imaging findings, miRNA quantitation revealed the presence of $\sim 4.4 \times 10^4$ copies of antimiR-21 (endogenously absent) and $\sim$ 4-fold increase in miR-100 (endogenously present) in the brains of mice treated with miRNA loaded T7 targeted CD-CS-polyGIONs. However, in the case of non-targeted CD-CS-polyGIONs-miRNAs, only 1.2×10^4 copies of antimiR-21 and ~1.9-fold increase in miR-100 expression were observed, pointing out that T7-mediated targeting strongly improved miRNA delivery. *Ex vivo* analysis of organs harvested from mice treated with T7 targeted polyGIONs indicated that although the majority of administered miRNAs effectively homed to GBMs in mice brains, significant fractions of these nanoparticles were also present in other major organs. Quantitative assessment of antimiR-21 levels in various organs indicated that small but significant fractions of miRNAs were present in lungs (17.73%), liver (9.4%), heart (1.4%), kidneys (2.4%), and spleen (3%) with respect to the quantities in the brain (100%). Thus, polyGIONs evaded the systemic first-pass effect, as well as the BBB, to deliver their therapeutic cargo selectively and in a targeted manner to orthotropically implanted GBMs in the brains of mice (Figure 6C, D).

Histology.

Typical H&E stains of brains obtained from untreated mice and mice co-treated with miRNA loaded polyGIONs plus TMZ are shown in Figure 7. In control animals, H&E stains showed large tumor cell populations characterized by dense nuclear distribution with higher instance of actively dividing nuclear morphology. On the other hand, H&E stained sections of treated brains revealed an interesting observation: at the core of the GBMs, there were

distinct regions of dead cells with radial propagations. Subsequent evaluation of these regions under a Cy5 filter of a fluorescence microscope showed the presence of Cy5 labelled miRNA specifically co- localized to this region of dead cells. This not only confirmed the successful delivery of miRNAs to GBMs using polyGIONs, but also provided evidence of their therapeutic efficacy in targeted growth arrest or reversal of GBMs in mice. These observations are in close agreement with those of the *in vivo* fluorescence imaging and the T1-weighted MRI intracranial imaging, denoting the selective accumulation of Cy5 labelled miRNAs and GION nanostars in the brain. H&E staining of the prefrontal cortex of the brain treated with miRNA-loaded polyGIONs did not show any instance of myelin vacuolation, a characteristic indication of neurotoxicity, when compared with the control groups. Furthermore, although polyGIONs partially accumulated in lungs upon intranasal administration, H&E staining revealed that they did not inflict any tissue damage in the lungs. That was also the case in other organs, i.e. liver, kidney, spleen and heart, after intranasal administration. The H&E stained sections of nasal mucosal epithelium from T7-CD-CS polyGIONs administered mice did not show any instance of toxicity or nasal congestion (Figure S8). The TUNEL staining of tumor tissues collected from controls and the animals treated with polyGION delivered Cy5-antimiR-21-miR-100 plus TMZ revealed significant enhancement in apoptosis in the tumors of animals treated with combination therapy compared to controls (Figure 7C). Overall, our results show efficient delivery of antimiR-21 and miR-100 corresponding to the intratumoral regions of cell death in GBM mouse models.

Conclusion.

There was a significant increase in survival of mice co-treated with T7-polyGIONs loaded with miR-100-antimiR-21 plus systemic TMZ, compared to the untreated control group, or the animals receiving polyGIONs-miR-100-antimiR-21, or TMZ alone. Once translated clinically, this novel theranostic nanoformulation and its associated intranasal delivery strategy could prove advantageous to GBM patients on many fronts, and with a strong potential to potentiate the effects of TMZ treatment in this difficult-to-treat malignancy.

Materials and Methods

Materials

We obtained all chemical reagents of 95% purity and above from Sigma-Aldrich (St. Louis, MO, USA) and used them without further purification. Specifically, we procured β-cyclodextrin, 1-adamantylamine, NHS-PEG-maleimide, dichloromethane, trimethylamine, NaOH, p-toluene sulfonyl chloride, acetonitrile, ammonium chloride, ethanol, ethylenediamine, chitin, LiCl, dimethylacetamide, acetone, methanol, and slide-a-lyzer cassettes. Ferrous chloride tetrahydrate ($FeCl_2 \cdot 4H_2O$) and Ferric chloride hexahydrate ($FeCl_3 \cdot 6H_2O$) were purchased from Sigma Aldrich (St Louis, USA), $H_3NO.HCl$ and NH_4OH was purchased from Alfa Aesar, HCl and tetramethylammonium hydroxide pentahydrate (98%) were obtained from Acros Organics (Thermo Scientific, USA), $HAuCl_4 \cdot 3H_2O$, NaOH and sodium citrate were obtained from Aldrich (St Louis, USA). MillQ water, purchased from Barnstead NANOpure (Thermo Scientific) system run at 18.2M resistance was used in the synthesis. Cy5 labeled antimiR-21 RNA-oligo and

miR-100 RNA-oligo were synthesized from Protein and Nucleic acid facility at Stanford (PAN, Stanford). Cell culture plates, FBS, penicillin, streptomycin, sodium bicarbonate, cell culture medium and phosphate-buffered saline (PBS) were purchased from GIBCO BRL (Frederick, MD).

Methods

Cell Culture.—We cultured U87-MG cells in Dulbecco's Modified Eagle's Medium supplemented with 10% FBS and 100 U/mL penicillin and 0.1% streptomycin in a 37 °C incubator with 5% CO_2 and 95% air. We tested the cells for any mycoplasma contamination using a MycoAlert kit from Lonza (Allendale, NJ), and maintained them at optimum culture conditions as per ATCC guidelines.

Synthesis of Chitosan-Cyclodextrin Hybrid Polymer: Synthesis of Mono-6-p-Toluenesulfonyl-Beta-Cyclodextrin (6-OTs-Beta-CD).—We added 1g of β-cyclodextrin to10 mL of NaOH (1% w/v) solution in a round bottom (RB) flask. The mixture was then placed on an ice water bath and stirred until it dissolved completely. To this solution we added 168 mg of p-toluene sulfonyl chloride (dissolved in 500 μl) of acetonitrile and continued stirring for another 2 h. After 2 h, the reaction was quenched with the addition of appropriate amount of ammonium chloride to bring the pH to 8. This resulted in the formation of a white precipitate, which was then washed with water and ethanol (twice) and vacuum dried.

Synthesis of Mono-6-(2-Aminoethyl)-Amino-6-Deoxy]-Beta-Cyclodextrin (CDen).—In a 3-neck RB flask we added 2 g of 6-OTS-beta-CD and the RB flask was connected to a reflux condenser and purged with nitrogen. To the RB flask we added excess of ethylenediamine and the reaction mixture to stirred for 5 h at 70 °C. The excess of ethylenediamine was then distilled under reduced pressure to obtain a pale-yellow solid. The obtained solid was then re-dissolved in a small amount of hot water, followed by precipitation with ethanol, filtration and vacuum drying.

Synthesis of 6-Tosylated Chitosan (CTN-6-OTs).—To 0.5 g of chitin, we added 1.4 g of LiCl and 26 mL of dimethylacetamide (DMAc) in a 3-neck RB flask. The reaction was stirred under inert nitrogen atmosphere to swell-up chitin. To this reaction, we added 7.8 mL of trimethylamine and 9 g of p-toluenesulfonyl chloride pre-dissolved in 26 mL of DMAc and stirred at 1000 rpm at 4 °C for 24 h and quenched the reaction by adding excess of acetone. The precipitate obtained was subsequently washed with methanol, water and ethanol, and vacuum dried.

Synthesis of Cyclodextrin Nitrogen Substituted Chitin Derivative (CTN-en-CD).—In a 3-neck RB flask protected under nitrogen we added 200 mg of CTN-6-OTs in 10 mL of 5% LiCl in DMAc and allowed to dissolve at 50 °C for 1–2 h. After complete dissolution, CDen was added to CTN-6-OTs at a mass ratio of 6:1. The reaction was stirred at 75 °C for 16 h. After reaction completion, we dialyzed the product against water for 7 days using a slide-a-lyzer cassette with a MWCO of 3500. The dialyzed (purified) product was lyophilized to obtain a pale-yellow powder.

Synthesis of Cyclodextrin Substituted Chitin Derivative (CTS-en-CD).—We added 200 mg of CTN-en-CD prepared from the previous step to 5 mL of 40% NaOH solution and stirred for 4 h while gradually heating the mixture to 110 °C. The crude product was then extracted by the addition of water to obtain a precipitate, which was further vacuum filtered. The resultant precipitate was repeatedly washed with water to attain a neutral pH and then dried under vacuum to obtain a pale brown powder.

Synthesis of Adamantane-PEG-T7 Peptide.—We used semipreparative HPLC reverse-phase column (Higgins, C18, 10 μm, 10 mm × 250 mm, 5 mL/min flow rate) for preparation and purification of T7 peptide. The mobile phase used for the purification of intermediate was 99.9% water + 0.1% TFA and 99.9% acetonitrile + 0.1% TFA. The eluent changed from 90% solvent A (H_2O) and 10% solvent B to 60% solvent A and 40% solvent B in 13 min and to 0 % solvent A and 100 % solvent B in 10 min. The product was collected at 8.7 min and concentrated by lyophilizer. For the synthesis of adamantane-PEG-T7 peptide conjugate, 1.5 equivalent of 1-adamantylamine, MW: 151.25 amine (sigma) was reacted with NHS-PEG-maleimide, MW: 2000 (Nanocs) in dichloromethane, and 1.5 equivalent of trimethylamine was added to the reaction mixture and incubated in ice for 30 min and then continued for 3 h under inert conditions. To the resultant solution, two equivalents of T7 peptide were added and the reactions continued to run overnight at RT under N_2 purging. The solution was dialyzed against water at 4 °C using slide-a-lyzer dialysis cassettes for 2 days and the water changed twice a day. The purified product was then lyophilized and the final molecular weight of the compound was determined through mass spec analysis.

Synthesis of GION Nanostars.—We prepared iron oxide nanoparticles (~15 nm) for GION nanostars synthesis by microwave assisted synthesis procedure. In brief, we dissolved $FeCl_2 \cdot 4H_2O$ (0.86 g) and $FeCl_3 \cdot 6H_2O$ (2.36 g) in 20 mL of deionized water preheated to 80–90 °C in a glass beaker. In another beaker, we dissolved 32 g PEG-400 in 20 mL of 0.8 M ammonia solution. The alkaline solution was then supplemented dropwise at 1 mL/min to ferrous solution under continuous stirring at 90°C. After the solution color turned from bright orange to black, the mixture was subsequently treated with microwave at 800W (2450 MHz) for 2.5 mins. The resultant black suspension of nanoparticles was magnetically separated and washed twice with deionized water followed by ethanol to remove unreacted components and then dried at 80 °C for 6 h in a vacuum.

The glassware used for the synthesis of GION nanoparticles was pretreated in aqua regia for 30 min, then washed and cleaned with double-distilled water under ultrasonication (3 min) thrice. Approximately 1 mg of as-prepared seed iron oxide nanoparticles were added to 5mL of an aqueous solution of TritonX-100 0.1 M (or 0.25 M) and 250 μL of $AgNO_3$ 0.004 M in water. Approximately 5 mL of $HAuCl_4$ (0.001 M) was then supplemented to the resulting mixture and stirred for 30 min at ~70 °C. After complete homogenous dissolution of all components, the solution temperature was brought down to 37 °C and 400 μL of an aqueous solution of ascorbic acid 0.0788 M were added. The aqueous solution was stirred for 30 min followed by dropwise addition of 0.6 mL of a previously ice-cooled solution of $NaBH_4$ 0.01 M solution. The mixture was constantly agitated at 1000 rpm resulting in a reddish-brown homogenous suspension which subsequently changed to intense green, and at this point the

reaction was stopped by reducing the temperature to ~4 °C. The resultant magnetic GION nanostars were magnetically separated and wash thrice with distilled water before using it for *in vivo* and *in vitro* studies.

MicroRNA Encapsulation in CD-CS and Synthesis of T7-PolyGION.—We used a stock miRNA concentration (10 nmol) diluted to 2 pmol/μL in DEPC water as the working concentration. We then used 1 μL of the working stock for encapsulation studies with increasing amounts of pre-synthesized chitosan-cyclodextrin conjugate polymers (stock 0.5 mg/mL in 2.5% acetic acid solution), i.e. 1 μg, 2 μg, 3 μg, 4 μg, 5 μg, 6 μg, and 7 μg, and the resultant volume was made up to 10 μL with DEPC water, and then incubated at 37 °C for 4 h. The complexes were loaded on 2% agarose gel and the electrophoresis run at 50 V for 45 min. After the run, the gel was imaged under IVIS Lumina-III In Vivo Imaging System with excitation at 675 nm and emission acquired for Cy5 filter.

The optimized miRNA loaded CD-CS was adapted for subsequent synthesis of polyGIONs. We used 1 nmol miRNA (5 of 200 pmol/μL stock) complexed with 2 mg of CD-CS (stock - 0.5 mg/mL) by incubating for 4 h at 30 °C in a mini tube rotator. The miRNA loaded CD-CS complex was then incubated with 400 μL (stock - 5 mg/mL) GIONs in a rotary incubator at 200 rpm overnight at 30 °C. Prior to co-incubation, as-prepared GION nanostars were dispersed in sterile DEPC treated water by brief probe sonication, i.e., 5 s "On" amplitude 40%, to form a 5 mg/mL uniform suspension of nanoparticles. The reaction mixture was then subjected to magnetic separation for 30 min and the resultant pellet was pooled together in a stipulated volume of 600 μL. Interaction of adamantane-PEG-T7 peptide conjugate to CD-CS-miR-GION was determined by the host-guest chemistry between CD and adamantane. Different weight ratios of adamantane-PEG-T7 peptide conjugate (Stock - 2.7 mg/mL), i.e. 1:1, 1:2 and 1:3 were added dropwise to the mixture of miRNA loaded CD-CS capped GIONs under constant agitation for 2 h at 4 °C in a mini tube rotator. The reaction mixture was then subjected to magnetic separation to harvest the T7 functionalized miR loaded poly GIONs. The resultant nanoparticles were resuspended in 600 μL DEPC treated water. The complexes were administered in 20 uL dosages at each time point of study.

The quantitative level of miRNA at each stage of synthesis procedure was assessed by qRT-PCR to deduce miRNA loading efficiency in the CD-CS-polyGIONs. The samples harvested at each stage were processed for microRNA extraction using a mirVana miRNA isolation kit and probed by TaqMan qRT-PCR analysis. The resulting qRT-PCR amplification plots were correlated with standard plots to arrive at specific miRNA copy number at each stage. On the other hand, the nanoparticle concentration and size distribution were deduced by a Nanoparticle Tracking Analyzer. The miRNA copy number was corroborated with NTA results to estimate miRNA loading efficiency in each particle.

The microRNA release study was carried out with stipulated quantity of CD-CS-polyGIONs in phosphate buffers of pH 5.5, pH 6.5, and pH 7.5 for 72 h on a rotary shaker. At the end of the respective time points (i.e. 8, 12, 24, 48 and 72 h) the nanoparticles were magnetically separated from the release medium and the fraction of miRNA in the release medium was subsequently quantified using TaqMan qRT-PCR analysis. The results were represented as

percentage miRNA release with respect to time for respective pH conditions relative to total input miRNA.

Nanoparticle Characterization.—We characterized each step of GION surface modification during the synthesis procedure for mean hydrodynamic diameters and zeta potential by dynamic light scattering (DLS) in a Malvern Zetasizer Nano Z system at 25 °C with a scattering angle of 90°. The ζ -potential (surface charge) of the GION based nanoparticles was determined by Smoluchowski approximation. Samples were prepared in PBS and diluted with deionized water to ensure that the measurements were performed under conditions of low ionic strength where the surface charge of the particles can be measured accurately. We characterized the particle size and morphology of the GION nanostars, CD-CS coated GIONs (polyGIONs), miRNA (antimiR-21 and miR-100) loaded CD-CS coated GIONs, and T7 functionalized miRNA loaded polyGIONs complexes using transmission electron microscopy (TEM, FEI-Tecnai G2 F20 X-TWIN). Images were acquired by an ORIUS CCD camera through digital micrography, and energy dispersive X-ray spectra (EDS) were recorded through the FEI-TIA interface. For sample preparation, 10 µL of polyGIONs suspension were drop casted on glow discharged copper grids with pure carbon support film, and incubated for 10–15 min and then washed with ultrapure water.

Evaluation of PolyGIONs Cellular Uptake.—We estimated cellular uptake of the polyGIONs both qualitatively and quantitatively using a fluorescence microscope and a flow cytometry analysis of cells treated with bare Cy5-antimiR-21, Cy5 tagged miR-100 loaded polyGIONs, and T7 functionalized miRNA loaded polyGIONs (1:1, 1:2 and 1:3). At 24 h, 48 h and 72 h we imaged the treated cells using an Olympus IX70 fluorescent microscope under differential interference contrast (DIC) and using a Cy5 filter. After acquiring representative images of each treatment, we trypsinized the cells and harvested them for flow cytometry analysis using a Guava® easyCyte Flow Cytometer at the end of 72 h period, for quantitative estimation of internalized Cy5 tagged miRNA fluorescence. We acquired about 5,000 events for each treatment condition, processed the results using FlowJo analysis software (Tree Star, Ashland, OR, USA), and represented the results as overlaid histograms of all treatment conditions.

As an alternative means of qualitative evaluation of polyGIONs, we performed Prussian blue staining upon treating U87-MG cells with polyGIONs functionalized with different extents of T7 peptide (i.e. 1:1, 1:2 and 1:3) for 72 h. Briefly, we fixed cells with 4% paraformaldehyde (PFA; AppliChem, Darmstadt, Germany) for 10 min at RT, and washed twice with phosphate buffered saline (PBS; Biochrom, Berlin, Germany). We incubated cells for 20 min in a mixture of 1% HCl (Carl Roth, Karlsruhe, Germany) and 2% potassium ferrocyanide (AppliChem) at equal volumes, washed twice with PBS and once with distilled water. Finally, we embedded cells in mounting medium (Permount, Sigma-Aldrich, USA) and imaged using a Nanozoomer (Hamamatsu, Japan) digital slide scanner.

RNA Extraction and qRT-PCR Analysis.—We extracted total RNA from treated U87-MG cells using a mirVana RNA extraction kit (Life technologies, Grand Island, NY) as per the manufacturer's protocol. In brief, control U87-MG cells and those treated with targeted and non-targeted polyGIONs loaded with antimiR-21 and miR-100 were lysed/homogenized

in 300 μL lysis buffer for 3 min at the end of the treatment period. We supplemented the lysis buffer with 30 μL of homogenate additive, and incubated at RT for 10 min. We extracted the RNA once with Phenol:Chloroform and purified it using a column washed with wash buffer and eluted in 50 μL of sterile distilled water. We quantified the total RNA and checked it for purity using a 2000 spectrophotometer (Thermo scientific). After quantification 15 ng of total RNA was reverse transcribed using RT-primers (Life technologies) using a reverse transcription kit (Life technologies) to produce corresponding cDNA. We carried out cDNA synthesis in a 15 μL reaction volume, and performed qRT-PCR using cDNA (5 ng of RNA equivalent) combined with TaqMan-PCR reagents (primer and probe mix). qRT-PCR was performed by 2 min incubation at 50 °C, followed by activation of the DNA polymerase at 95 °C for 10 min, 60 cycles of 95 °C for 15 s, and 60 °C for 60 s in an Eppendorf Real flex qRT-PCR system (Eppendorf AG, Hamburg, Germany). The qRT-PCR reaction was carried out in a 20 μL reaction volume. We calculated the expression of miRNA using the $2^{-\Delta\Delta CT}$ method.

Cell Viability Analysis using PI Staining.—We evaluated the efficiency of polyGION-mediated delivery of miRNA and presensitization of U87-MG cells to TMZ therapy in U87-MG cells at 48 h and 72 h, in the absence or presence of TMZ. We seeded U87-MG cells at a density of 150,000 in each well of a 6-well plate and treated with equivalent amounts of bare polyGIONs, or T7 targeted polyGIONs loaded with antimiR-21 or miR-100, or both miRNAs. On the following day we supplemented two different concentrations of TMZ for every polyGION treatment condition, for the next 48 h and 72 h. At the end of these treatment periods, cells we collected the cells by trypsinization and fixed them in ice-cold 70% ethanol. The fixed cells were washed and stained with PI (15 nM) in the presence of RNase A (10 mg/mL) and 0.01% Triton X100 (Life Technologies, Grand Island, NY, USA). We acquired 5,000 events for each treatment condition and represented the results as histograms with percentage of live and apoptotic cells.

Immunoblot Analysis.—To determine the delivery and downstream effects of antimiR-21 and miR-100 in the presence and absence of TMZ, we carried out immunoblot analysis using target protein specific antibodies. We seeded 50,000 U87-MG cells in 12-well plates and treated with equivalent amounts of T7 targeted polyGIONs loaded with either antimiR-21 or miR-100 or with both in the presence or absence of TMZ. After 48 h of treatment, we harvested cells and processed them further for immunoblot analysis with anti-TK antibody. In brief, we lysed cells in 100 mL lysis buffer, and mixed 80 μg of total protein from treated U87-MG cells with β-mercaptoethanol (Bio-Rad) and 10 μL of NuPAGE LDS (4X) loading buffer, then heated at 95 °C for 5 min and loaded in 4–12% SDS-polyacrylamide gel electrophoresis gradient gel (Invitrogen), and run at 80 V for 2 h. The resolved proteins from the gel were then electroblotted onto a 0.2 μm pore-size nitrocellulose membrane (Schleicher & Schuell, Keene, NH, USA). We blocked the membrane with 5% non-fat dry milk in tris-buffered saline containing 0.01% Tween-20 (TBS-T, pH 7.6) for 30 min and incubated with the appropriate polyclonal antibody overnight at 4 °C on a rocking platform. On the following day, we replaced the primary antibody with peroxidase-conjugated goat anti-rabbit IgG secondary antibody (1:10 000 dilution, Rockland Immunochemicals, Gilbersville, PA, USA). After washing it thrice for 10

min in TBS-T buffer, and allowing it to rock for 2 h, we then developed the blots using Pierce ECL Western Blotting Substrate (Thermo Fisher Scientific, USA) and imaged and quantified them using an IVIS Lumina III *In Vivo* Imaging System.

***In Vivo* Intranasal Administration of PolyGIONs.—**We performed all animal experiments under the guidance of the Administrative Panel on Laboratory Animal Care (APLAC), Stanford University. We obtained all nude mice (Nu/Nu) from Charles River laboratories (Wilmington, MA). We performed the intranasal delivery of nanoparticle formulation in mice under mild sedation, using isoflurane gas anesthesia, to enable animal recovery within a couple of minutes. We placed each animal in the induction chamber and adjusted the oxygen flowmeter to 0.8 to 1.5 L/minute. Once completely sedated, we placed each mouse parallel to the tabletop in the head back position to monitor for a steady breathing rate. We then administered 20 μL of the nanoformulation intranasally as 5 μL/drop over 15–20 min. After administering each drop, we stopped for 3–4 min to ensure the animal inhaled the drop and that it was breathing at a steady rate. The nostrils were observed closely for signs of blockage or irritation. After administering the full dose, each animal was allowed to recover from anesthesia before transfer to its cage.

Stereotaxic Intracranial Implantation of GBM in Mice.—We surgically created a burr hole 3 mm lateral and 1 mm rostral to bregma, using a small drill (1 mm diameter). After positioning the needle tip at the lower aspect of the cerebrum, within 3 min we injected approximately 5×10^5 GBM cells (stable FLuc-EGFP expressing cells) suspended in 3 μL PBS using a graduated Hamiltonian syringe. We left the needle in place for a minute after the end of cell inoculation, and then removed it slowly. The inoculation site was sterilized with alcohol swabs, and the scalp sutured.

Fluorescence and Bioluminescence Imaging.—To acquire Cy5-fluorescence images (at 605/645 nm) and tumor bioluminescence images at predetermined time points of the study, we first anesthetized the mice through a nose cone using 2% isoflurane in oxygen. We then imaged the mice using a Lago spectral instruments imaging system (Tucson, AZ). After one week of intracranial GBM implantation, the tumor bioluminescence was considered as the baseline and then mice were randomized into groups and inducted into the treatment protocols. We administered TMZ intraperitonially, and polyGIONs intranasally at specific time points as indicated in the schematic (Scheme 1). At every time point, tumor bioluminescence was tracked upon intraperitoneal administration of the substrate D-Luciferin (3mg). We also recorded the mouse weight at each time point and thereafter for 39 days. We sacrificed all animals on Day 39, and we collected the organs and tumors for *ex vivo* quantification of miRNA delivery and histological analysis.

Head microCT scans.—The intranasal route of polyGION migration into the brain was traced using high-resolution microCT. The mice were scanned before injection to determine the CT baseline, followed by imaging after 48 h post administration of three doses of polyGIONs. The scans were performed with a vivaCT 40 (SCANCO Medical AG, Switzerland) *in vivo* microCT operating at 70 kVp and 112 μA. The images were acquired over 1000 slices and co-registered with pre-administration scan for subsequent analysis.

Hematoxylin and Eosin Staining.—After completing the study, we fixed the excised tissues in 4% paraformaldehyde overnight at 4 °C, immersed them in 70% ethanol, embedded them in paraffin, and then sliced at 5 μm thickness using a Leica cryo-microtome (Leica RM2255). We stained these sections in undiluted hematoxylin (Sigma-Aldrich, USA) for 2 min, rinsed in running water, and differentiated in 1% HCl acid/alcohol for 30 s. We then washed these and immersed them in bluing solution (Fisher, USA) for 1 min, washed in running water and rinsed in 10 dips of 95% alcohol. After this, we counterstained the slides in eosin by dipping into 1:5 ethanol diluted eosin solution (Fisher) for less than 30 s, dehydrated through 95% alcohol, and then xylene for 5 min each. We mounted slides with xylene based mounting medium (Permount, Sigma-Aldrich, USA) and imaged using Nanozoomer (Hamamatsu, Japan).

Bone Decalcification, H&E and Prussian Blue Staining of Mouse Head

At the end of treatment time point, the mice were sacrificed, and their heads were harvested intact, de-skinned and immersed in mild decalcifying solution Cal Ex II (composed of formic acid (decalcifying agent) and formalin (fixative agent)) for 72 hours. After the incubation the decalcified skulls were transferred to 70% ethanol and embedded in paraffin and used for sectioning. The paraffin embedded heads were sectioned into slices of 5 μm thickness. The processed slices were then used for H&E (as mentioned above) and Prussian blue staining. For iron staining, the slides were deparaffinized and processed by Prussian Blue Test Kit (Sigma Aldrich) as per manufacturers protocol.

TUNEL Staining for Apoptosis Measurement.—We assessed the U87-MG orthotropic GBM xenografts of mice treated with different versions of polyGIONs in combination with TMZ, for anti-proliferative effects by visualizing apoptotic cells in a TUNEL assay. For this, a portion of the tumor was frozen in OCT (TissueTek) and sectioned to 10 μm using a cryomicrotome (Leica CM1850, Wetzlar, Germany). We performed a terminal deoxynucleotidyl transferase (TdT) nick-end labeling (TUNEL) assay using a Trevigen TACS 2 TdT-DAB (diaminobenzidine) *in situ* Apoptosis Detection Kit (TREVIGEN, Gaithersburg, MD, USA) according to the manufacturer's instructions. After staining, we scanned the slides in a Nanozoomer 2.0RS (Hamamatsu, Japan) digital scanner and assessed for diaminobenzidine staining of apoptotic cells using Nanozoomer Digital Pathology software.

Statistical Analyses.—We performed Student's t-test for all statistical analyses. *P*-values were determined, and differences considered statistically significant when the *P*-value was less than 0.05.

Supplementary Material

Refer to Web version on PubMed Central for supplementary material.

Acknowledgements

REFERENCES

[1]. Lehrer S, Green S, Ramanathan L, Rosenzweig K, Labombardi V, No consistent relationship of glioblastoma incidence and cytomegalovirus seropositivity in whites, blacks, and Hispanics, Anticancer research 32(3) (2012) 1113–5. [PubMed: 22399642]

[2]. Stupp R, Mason WP, van den Bent MJ, Weller M, Fisher B, Taphoorn MJ, Belanger K, Brandes AA, Marosi C, Bogdahn U, Curschmann J, Janzer RC, Ludwin SK, Gorlia T, Allgeier A, Lacombe D, Cairncross JG, Eisenhauer E, Mirimanoff RO, Radiotherapy plus concomitant and adjuvant temozolomide for glioblastoma, The New England journal of medicine 352(10) (2005) 987–96. [PubMed: 15758009]

[3]. Johnson DR, O'Neill BP, Glioblastoma survival in the United States before and during the temozolomide era, Journal of Neuro-Oncology 107(2) (2012) 359–364. [PubMed: 22045118]

[4]. Pardridge WM, The blood-brain barrier: bottleneck in brain drug development, NeuroRx : the journal of the American Society for Experimental NeuroTherapeutics 2(1) (2005) 3–14. [PubMed: 15717053]

[5]. Malhotra M, Toulouse A, Godinho BMDC, Mc Carthy DJ, Cryan JF, O'Driscoll CM, RNAi therapeutics for brain cancer: current advancements in RNAi delivery strategies, Molecular BioSystems 11(10) (2015) 2635–2657. [PubMed: 26135606]

[6]. Macfarlane LA, Murphy PR, MicroRNA: Biogenesis, Function and Role in Cancer, Curr Genomics 11(7) (2010) 537–61. [PubMed: 21532838]

[7]. Lane DP, Cancer. p53, guardian of the genome, Nature 358(6381) (1992) 15–6. [PubMed: 1614522]

[8]. Devulapally R, Sekar NM, Sekar TV, Foygel K, Massoud TF, Willmann JK, Paulmurugan R, Polymer nanoparticles mediated codelivery of antimiR-10b and antimiR-21 for achieving triple negative breast cancer therapy, ACS Nano 9(3) (2015) 2290–302. [PubMed: 25652012]

[9]. Karsy M, Arslan E, Moy F, Current Progress on Understanding MicroRNAs in Glioblastoma Multiforme, Genes Cancer 3(1) (2012) 3–15. [PubMed: 22893786]

[10]. Moller HG, Rasmussen AP, Andersen HH, Johnsen KB, Henriksen M, Duroux M, A systematic review of microRNA in glioblastoma multiforme: micro-modulators in the mesenchymal mode of migration and invasion, Mol Neurobiol 47(1) (2013) 131–44. [PubMed: 23054677]

[11]. Yang CH, Yue J, Pfeffer SR, Fan M, Paulus E, Hosni-Ahmed A, Sims M, Qayyum S, Davidoff AM, Handorf CR, Pfeffer LM, MicroRNA-21 promotes glioblastoma tumorigenesis by down-regulating insulin-like growth factor-binding protein-3 (IGFBP3), J Biol Chem 289(36) (2014) 25079–87. [PubMed: 25059666]

[12]. Rao SA, Santosh V, Somasundaram K, Genome-wide expression profiling identifies deregulated miRNAs in malignant astrocytoma, Mod Pathol 23(10) (2010) 1404–17. [PubMed: 20711171]

[13]. Alrfaei BM, Vemuganti R, Kuo JS, microRNA-100 targets SMRT/NCOR2, reduces proliferation, and improves survival in glioblastoma animal models, PLoS One 8(11) (2013) e80865.

[14]. Li C, Gao Y, Zhang K, Chen J, Han S, Feng B, Wang R, Chen L, Multiple Roles of MicroRNA-100 in Human Cancer and its Therapeutic Potential, Cell Physiol Biochem 37(6) (2015) 2143–59. [PubMed: 26606597]

[15]. Ory B, Ellisen LW, A microRNA-dependent circuit controlling p63/p73 homeostasis: p53 family cross-talk meets therapeutic opportunity, Oncotarget 2(3) (2011) 259–64. [PubMed: 21436470]

[16]. Degenhardt Y, Greshock J, Laquerre S, Gilmartin AG, Jing J, Richter M, Zhang X, Bleam M, Halsey W, Hughes A, Moy C, Liu-Sullivan N, Powers S, Bachman K, Jackson J, Weber B, Wooster R, Sensitivity of cancer cells to Plk1 inhibitor GSK461364A is associated with loss of p53 function and chromosome instability, Mol Cancer Ther 9(7) (2010) 2079–89. [PubMed: 20571075]

[17]. Guan R, Tapang P, Leverson JD, Albert D, Giranda VL, Luo Y, Small interfering RNA-mediated Polo-like kinase 1 depletion preferentially reduces the survival of p53-defective, oncogenic

transformed cells and inhibits tumor growth in animals, Cancer Res 65(7) (2005) 2698–704. [PubMed: 15805268]

[18]. Louis DN, Perry A, Reifenberger G, von Deimling A, Figarella-Branger D, Cavenee WK, Ohgaki H, Wiestler OD, Kleihues P, Ellison DW, The 2016 World Health Organization Classification of Tumors of the Central Nervous System: a summary, Acta Neuropathol 131(6) (2016) 803–20. [PubMed: 27157931]

[19]. Groothuis DR, The blood-brain and blood-tumor barriers: a review of strategies for increasing drug delivery, Neuro Oncol 2(1) (2000) 45–59. [PubMed: 11302254]

[20]. Mc Carthy DJ, Malhotra M, O'Mahony AM, Cryan JF, O'Driscoll CM, Nanoparticles and the blood-brain barrier: advancing from in-vitro models towards therapeutic significance, Pharm Res 32(4) (2015) 1161–85. [PubMed: 25446769]

[21]. Oller-Salvia B, Sanchez-Navarro M, Giralt E, Teixido M, Blood-brain barrier shuttle peptides: an emerging paradigm for brain delivery, Chem Soc Rev 45(17) (2016) 4690–707. [PubMed: 27188322]

[22]. Malhotra M, Tomaro-Duchesneau C, Saha S, Prakash S, Intranasal, siRNA Delivery to the Brain by TAT/MGF Tagged PEGylated Chitosan Nanoparticles, J Pharm (Cairo) 2013 (2013) 812387. [PubMed: 26555995]

[23]. Hashizume R, Ozawa T, Gryaznov SM, Bollen AW, Lamborn KR, Frey WH 2nd, Deen DF, New therapeutic approach for brain tumors: Intranasal delivery of telomerase inhibitor GRN163, Neuro Oncol 10(2) (2008) 112–20. [PubMed: 18287341]

[24]. Thorne RG, Pronk GJ, Padmanabhan V, Frey WH, 2nd, Delivery of insulin-like growth factor-I to the rat brain and spinal cord along olfactory and trigeminal pathways following intranasal administration, Neuroscience 127(2) (2004) 481–96. [PubMed: 15262337]

[25]. Calzolari A, Larocca LM, Deaglio S, Finisguerra V, Boe A, Raggi C, Ricci-Vitani L, Pierconti F, Malavasi F, De Maria R, Testa U, Pallini R, Transferrin receptor 2 is frequently and highly expressed in glioblastomas, Transl Oncol 3(2) (2010) 123–34. [PubMed: 20360937]

[26]. Bhowmik A, Khan R, Ghosh MK, Blood brain barrier: a challenge for effectual therapy of brain tumors, Biomed Res Int 2015 (2015) 320941. [PubMed: 25866775]

[27]. Valdes-Rives SA, Casique-Aguirre D, German-Castelan L, Velasco-Velazquez MA, Gonzalez-Arenas A, Apoptotic Signaling Pathways in Glioblastoma and Therapeutic Implications, Biomed Res Int 2017 (2017) 7403747. [PubMed: 29259986]

[28]. Wei X, Wang W, Wang L, Zhang Y, Zhang X, Chen M, Wang F, Yu J, Ma Y, Sun G, MicroRNA-21 induces 5-fluorouracil resistance in human pancreatic cancer cells by regulating PTEN and PDCD4, Cancer Med 5(4) (2016) 693–702. [PubMed: 26864640]

[29]. Sasmita AO, Wong YP, Ling APK, Biomarkers and therapeutic advances in glioblastoma multiforme, Asia Pac J Clin Oncol 14(1) (2018) 40–51. [PubMed: 28840962]

[30]. Inaba N, Kimura M, Fujioka K, Ikeda K, Somura H, Akiyoshi K, Inoue Y, Nomura M, Saito Y, Saito H, Manome Y, The effect of PTEN on proliferation and drug-, and radiosensitivity in malignant glioma cells, Anticancer research 31(5) (2011) 1653–8. [PubMed: 21617223]

[31]. Endersby R, Baker SJ, PTEN signaling in brain: neuropathology and tumorigenesis, Oncogene 27(41) (2008) 5416–30. [PubMed: 18794877]

[32]. Hirose Y, Berger MS, Pieper RO, p53 effects both the duration of G2/M arrest and the fate of temozolomide-treated human glioblastoma cells, Cancer Res 61(5) (2001) 1957–63. [PubMed: 11280752]

[33]. Caporali S, Falcinelli S, Starace G, Russo MT, Bonmassar E, Jiricny J, D'Atri S, DNA damage induced by temozolomide signals to both ATM and ATR: role of the mismatch repair system, Mol Pharmacol 66(3) (2004) 478–91. [PubMed: 15322239]

[34]. Mucignat-Caretta C, Redaelli M, Caretta A, One nose, one brain: contribution of the main and accessory olfactory system to chemosensation, Front Neuroanat 6 (2012) 46. [PubMed: 23162438]

[35]. Xiao C, Davis FJ, Chauhan BC, Viola KL, Lacor PN, Velasco PT, Klein WL, Chauhan NB, Brain transit and ameliorative effects of intranasally delivered anti-amyloid-beta oligomer antibody in 5XFAD mice, J Alzheimers Dis 35(4) (2013) 777–88. [PubMed: 23542865]

[36]. Veening JG, Barendregt HP, The regulation of brain states by neuroactive substances distributed via the cerebrospinal fluid; a review, Cerebrospinal Fluid Res 7 (2010) 1. [PubMed: 20157443]

[37]. Kao YY, Cheng TJ, Yang DM, Wang CT, Chiung YM, Liu PS, Demonstration of an olfactory bulb-brain translocation pathway for ZnO nanoparticles in rodent cells in vitro and in vivo, J Mol Neurosci 48(2) (2012) 464–71. [PubMed: 22528453]

[38]. Raghnaill MN, Bramini M, Ye D, Couraud PO, Romero IA, Weksler B, Aberg C, Salvati A, Lynch I, Dawson KA, Paracrine signalling of inflammatory cytokines from an in vitro blood brain barrier model upon exposure to polymeric nanoparticles, Analyst 139(5) (2014) 923–30. [PubMed: 24195103]

[39]. Ong WY, Shalini SM, Costantino L, Nose-to-brain drug delivery by nanoparticles in the treatment of neurological disorders, Curr Med Chem 21(37) (2014) 4247–56. [PubMed: 25039773]
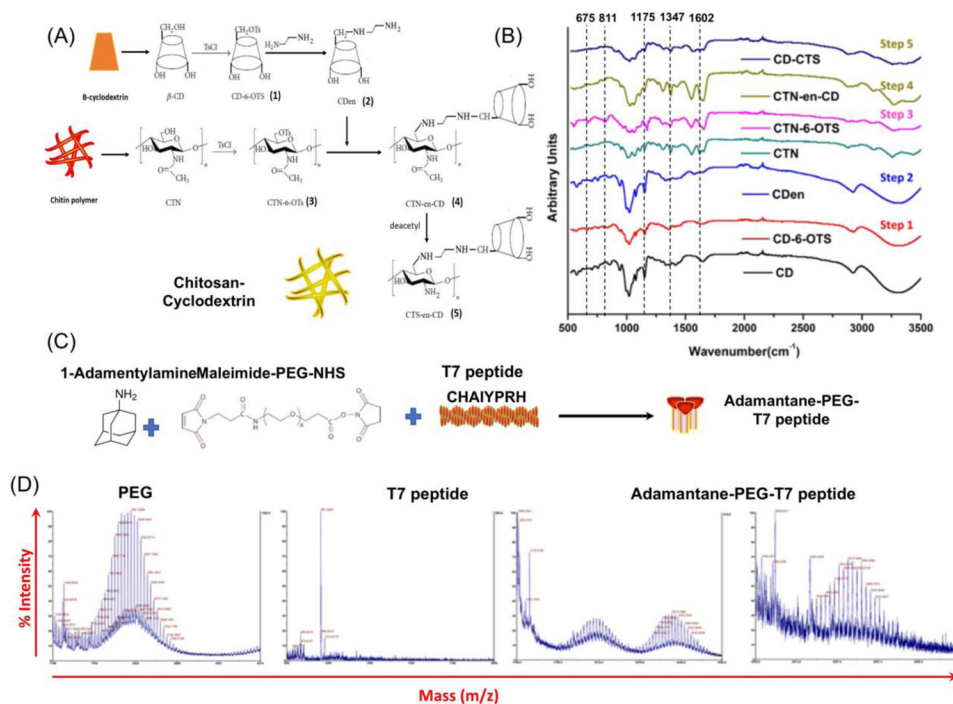
Figure 1.
(**A**) Sequence of reactions involved in synthesis of cyclodextrin conjugated chitosan (CD-CS) hybrid polymer; (**B**) FTIR spectra of each intermediate obtained in the 5 step CD-CS synthesis process; (**C**) Schematic representation of reaction chemistry for the synthesis of adamantane-PEG-T7 conjugate; (**D**) MALDI-TOF analysis of as-synthesized T7-peptide and its conjugation to PEG-adamantane.
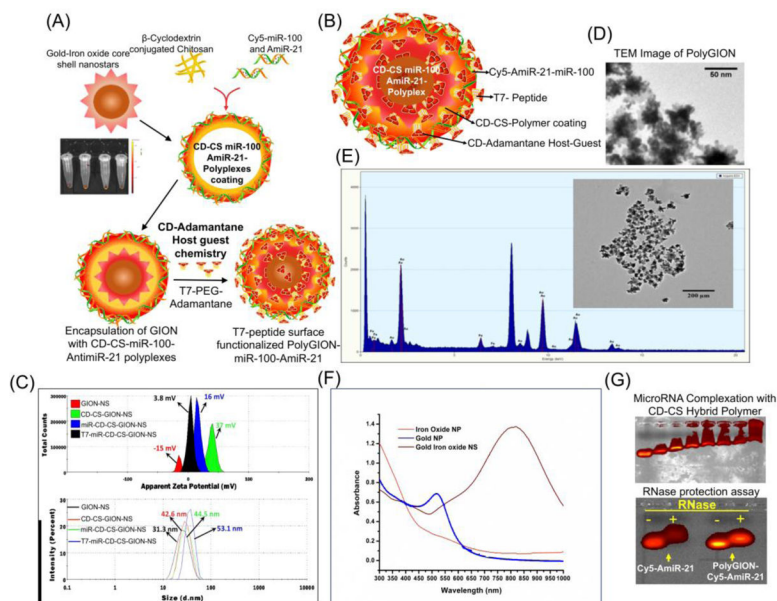
Figure 2.
(A) Schematic illustration of synthesis of PolyGIONs and fluorescence images of Cy5 labelled miR-100 and antimiR-21 loaded CD-CS complexes. **(B)** Schematic representation of as-prepared polyGIONs structure and their various compositions. **(C)** DLS measuring zeta potential and size of nanoparticles after each step of GION surface modification. **(D)** TEM micrograph of GION. **(E)** GION coated with miR-100/antimiR-21 encapsulated CD-CS polymer layer, its EDS analysis, and corresponding images. **(F)** UV-Vis spectra of as-prepared GION NS and its precursor nanoparticles. **(G)** Gel retardation assay for Cy5-miR-100/antimiR-21 encapsulation in CD-CS hybrid polymer and RNase protection assay for measuring the stability of encapsulated miRNAs in polyGION-CD-CS.
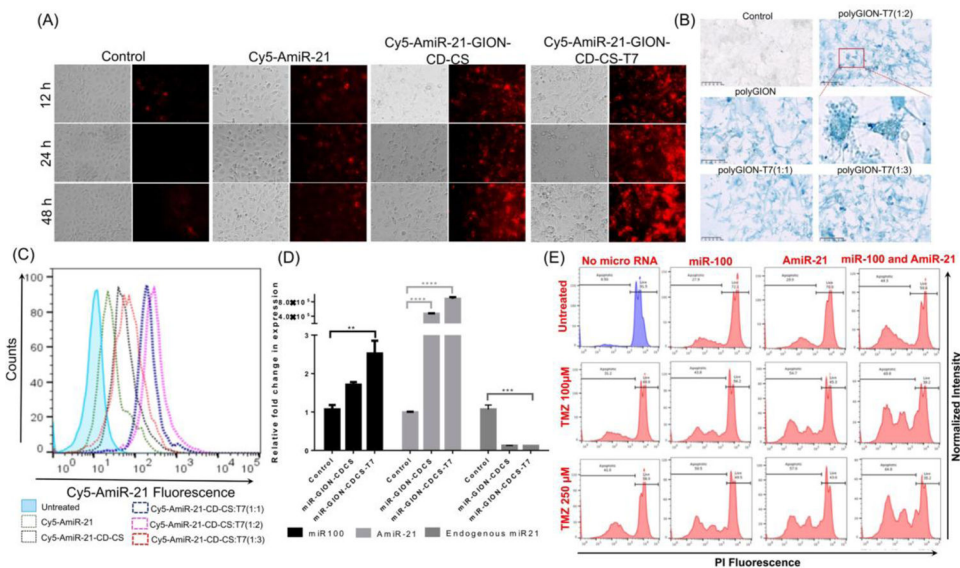
Figure 3.
PolyGIONs uptake by U87-MG cells: **(A)** Cy5-miRNA fluorescence under a microscope at 12 h, 24 h and 48 h. **(B)** Concentration dependent uptake of GIONs by Prussian blue staining. **(C)** Flow cytometer analysis for Cy5-antimiR-21 fluorescence at 48 h post treatment. **(D)** Fold change in miRNA expression levels 48 h after transfection. **(E)** Live-dead analysis of U87-MG cells treated with different combinations of miRNA and temozolamide (TMZ). The data are presented as mean ± SEM; * represents p<0.05, ** represents p<0.01, *** represents p<0.001and **** represents p<0.0001.
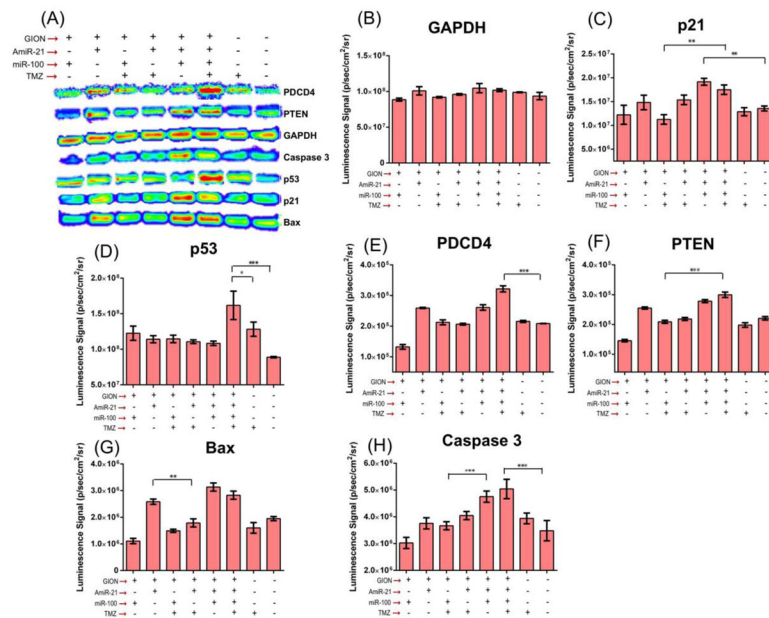
Figure 4.
(A) Immunoblot analysis of target proteins and downstream cell signaling pathways, and **(B–H)** quantitative change in expression of **(B)** GAPDH; **(C)** p21; **(D)** p53; **(E)** PDCD4; **(F)** PTEN; **(G)** Bax and **(H)** Caspase-3. The data are presented as mean ± SEM; * represents p<0.05, ** represents p<0.01 and *** represents p<0.001.

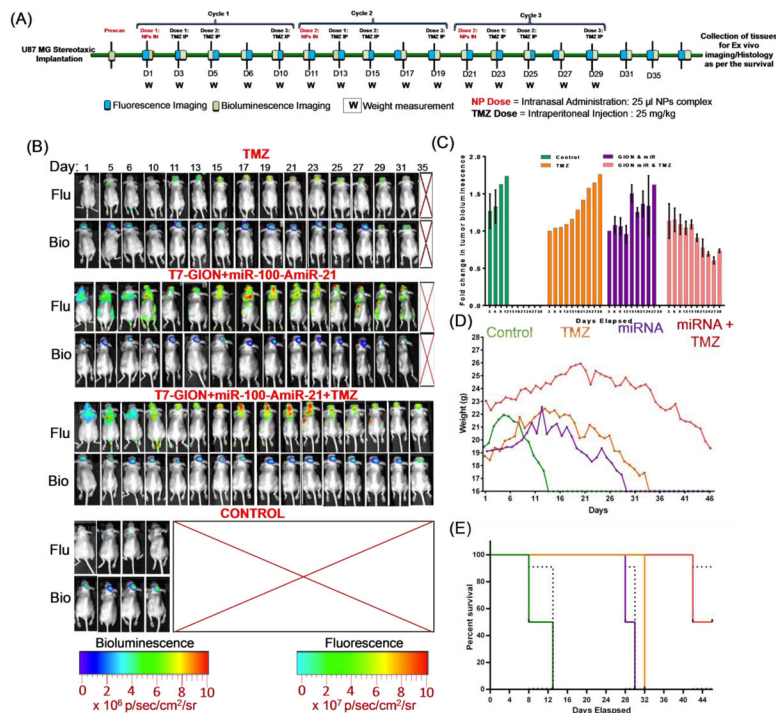**Figure 5.**
(A) Schematic outline shows the In vivo experimental design for treatments and imaging timelines; **(B)** Fluorescence (Cy5-miRNA loaded nanoparticles) and bioluminescence (FLuc-EGFP expressing GBM) images acquired at different time points after treatment, using a Lago-X *in vivo* imaging system; **(C)** Quantitative graph showing the tumor bioluminescence measured with respect to treatment duration; **(D)** Mice weight profiles over the treatment duration and their **(E)** survival curve (Gehan-Breslow-Wilcoxon).
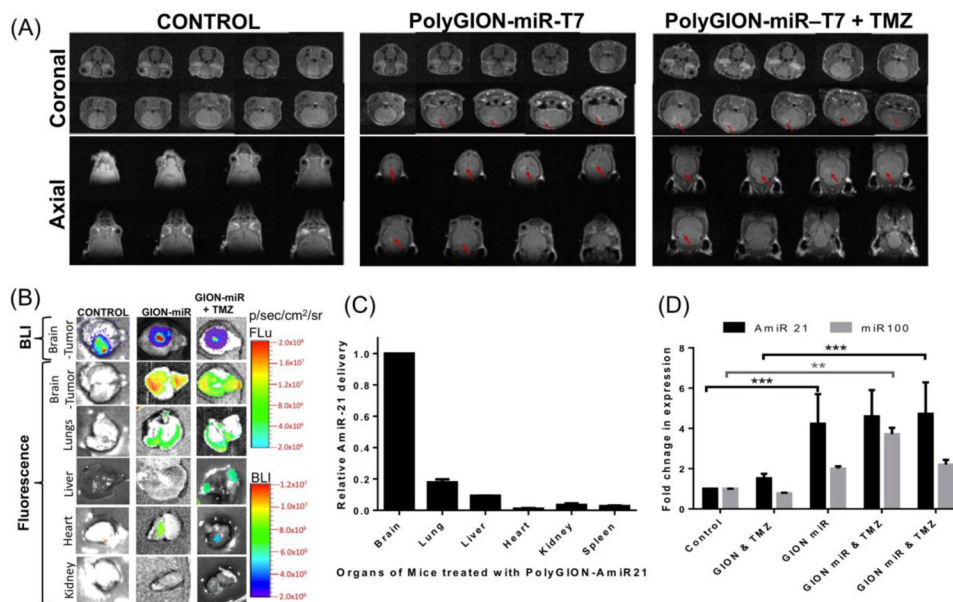
Figure 6.
(A) 3T MRI head scans (coronal and axial) of mice treated with PolyGIONs-miRNAs. **(B–D)** Biodistribution of miRNA in mice brains and other major organs using **(B)** *ex vivo* fluorescence imaging and **(C)** RT-PCR quantification of miRNA distribution in various organs of PolyGION-CD-CS-miRNA-T7 treated mice; **(D)** Quantification of antimiR-21 and miR-100 levels in brains of various treatment groups using RT-PCR. The data are presented as mean ± SEM; * represents p<0.05, ** represents p<0.01 and *** represents p<0.001.
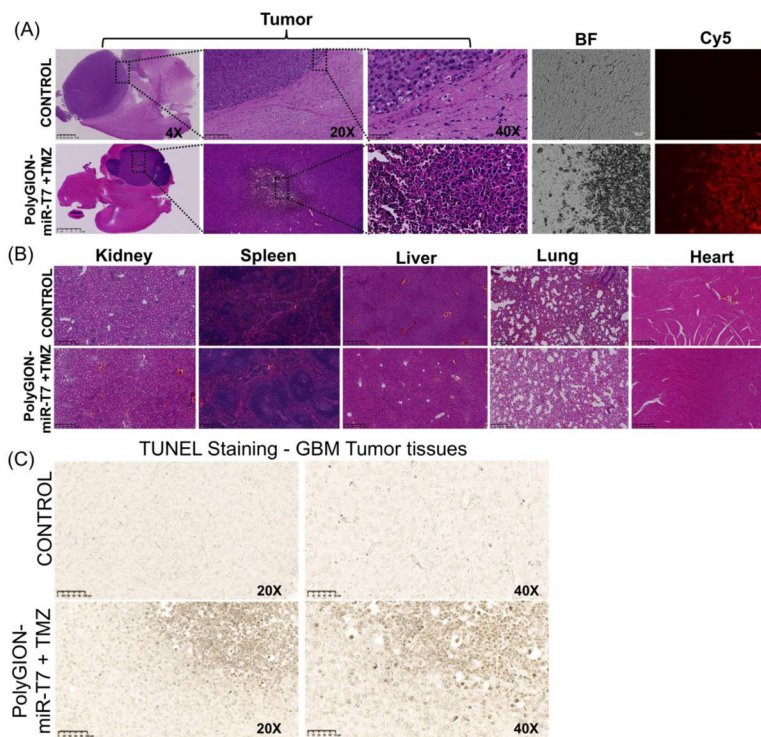
Figure 7.
Histological analysis of tumors and different organs assessed for toxicity and treatment effect using Hematoxylin and Eosin (H&E) staining and fluorescence imaging. **(A)** U87-MG orthotopic tumor in the brain after H&E staining, and closer look for the polyGION delivered Cy5-antimiR-21-miR-100 using fluorescence microscopy; and **(B)** H&E staining of different organs from treatment groups for toxicity assessment (kidney, spleen, liver, lung and heart). **(C)** TUNEL staining results of tumor tissues from control and the animals treated with a polyGION delivered Cy5-antimiR-21-miR-100 plus TMZ used for the study.
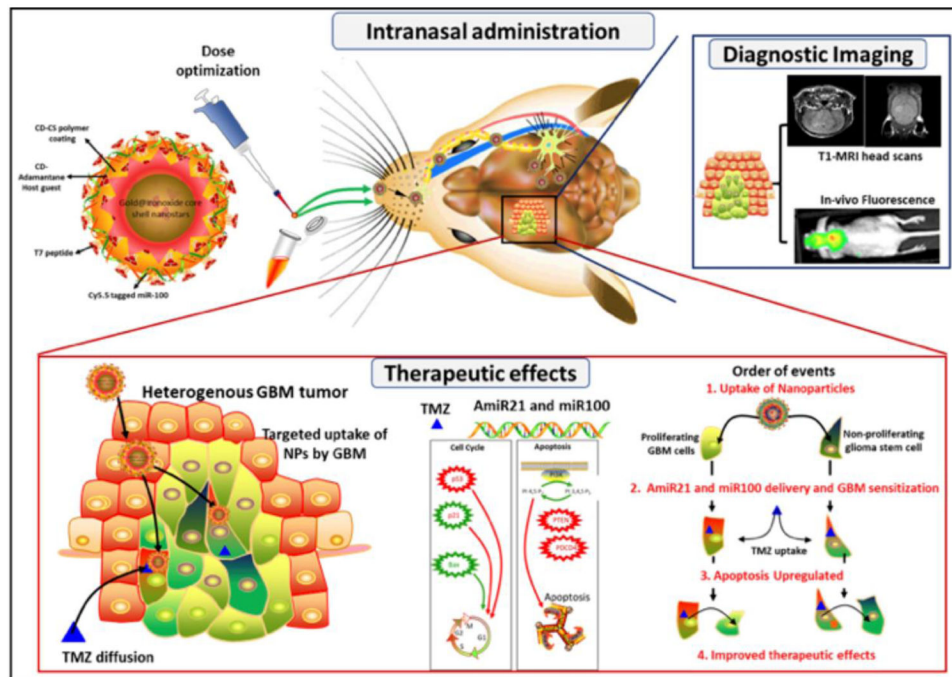
Scheme 1.
Schematic illustration of the principle of intranasal polyGION-miRNAs delivery and its theranostic imaging and therapeutic effect in GBM *in vivo*.

Table 1:

Quantitative estimation of miRNA loading efficiency at each stage of synthesis.

Sample	RT-PCR (Ct)	Dilution Factor	Absolute Copy No.	miRNA (%)	GION	miR/GION NP
Total miR (Input)			6.022×10^{14}	100%		
miR loaded CD-CS	16.14878	4800	4.6973×10^{14}	78.0029%		
CD-CS-GION (Supernatant)	20.72669	14980	2.59643×10^{13}	5.527%		
CD-CS GION (Nanoparticle)	14.3345	3207	3.89341×10^{14}	82.8856% ± 8.14	6.06×10^{10}	6424 ± 83
T7-CD-CS polyGION	14.25248	3207	4.18277×10^{14}	89.0456% ± 12.34%	6.2×10^{10}	6746± 134